NUMERICAL MICROLOCAL ANALYSIS BY FAST GAUSSIAN WAVE PACKET TRANSFORMS AND APPLICATION TO HIGH-FREQUENCY HELMHOLTZ PROBLEMS*

CHI YEUNG LAM† AND JIANLIANG QIAN†

Abstract. We develop a novel numerical microlocal analysis (NMLA) method using fast Gaussian wave packet transforms. Our new NMLA method extracts ray directions at discrete locations by analyzing highly oscillatory wavefields with fast Gaussian wave packet transforms. Theoretically, to achieve the same accuracy, the novel NMLA has the same time complexity as the original NMLA, which is based on local plane-wave analysis for Helmholtz problems, but the new NMLA is applicable to generic oscillatory wavefields and is straightforward to implement. We apply the new NMLA to high-frequency Helmholtz problems, so that we are able to extract directions from a reduced-frequency solution and further incorporate these directions into a ray-based interior-penalty discontinuous Galerkin method to solve for high-frequency solutions. In this way, we observe no apparent pollution effects. We provide numerical results in 2 dimensions to justify the claims.

Key words. microlocal analysis, fast Gaussian wave packet transform, geometrical optics, Helmholtz equations

AMS subject classifications. 78A05, 78A46, 78M35

DOI. 10.1137/18M1218078

1. Introduction. In mathematical analysis, microlocal analysis consists of Fourier-transform related techniques for analyzing variable-coefficient partial differential equations, including Fourier integral operators, wavefront sets, and oscillatory integral operators, so that such analysis allows localized scrutiny not only with respect to location in space but also with respect to cotangent directions at a given point [1]. Since wave singularities propagate along characteristics, applying microlocal analysis to spatial wave fields will reveal cotangent-space related characteristic (or ray) information at each spatial point [2, 3, 4, 5]. Moreover, such localized ray information can be incorporated into a finite element basis so that one can design effective numerical methods to solve wave equations [6, 7, 8, 9]. In this paper, we propose to develop a new numerical microlocal analysis (NMLA) method by applying fast Gaussian wave packet transforms [3] to analyze oscillatory wave fields, which yields ray directions at each spatial point; we further incorporate these ray directions into interior-point discontinuous Galerkin methods for Helmholtz equations to develop efficient numerical methods which are uniformly convergent with respect to the wave number as it becomes larger.

The notion of numerical microlocal analysis method was first proposed in [2]. *Assuming* that the to-be-processed data are solutions of the Helmholtz equations, the authors in [2] designed a Jabobi–Anger expansion and Fourier-transform based plane-wave analysis method to process Dirichlet observables collected on a sphere around each to-be-analyzed point. Later, authors in [10] improved the method in

---

†Department of Mathematics, Michigan State University, East Lansing, MI 48824 (lamchiye@msu.edu, jqian@msu.edu).

[2] by using L^1 minimization instead of Tichonov regularization to obtain much less noise-sensitive results. To overcome stability issues and improve accuracy in identified ray directions, the method in [2] was further developed in [5] to analyze impedance observables in a similar setup; to deal with multiple plane waves or point sources arriving at an observation point, the authors of [5] further developed a decomposition filter with Gaussian weights. The NMLA method is used for numerically and locally finding crossing rays and their directions from samples of wavefields [2, 5]. Compared to other methods, such as Prony's method [11] and the matrix pencil method [12], that perform similar tasks, the NMLA is simpler and more robust.

In comparison to the approaches in [2, 5], our NMLA is much more straightforward and easy to implement in the sense that we apply fast Gaussian wave packet transforms directly to the given oscillatory wavefield, where we *neither assume* the underlying model being Helmholtz *nor preprocess* the input data into Dirichlet or impedance data on a certain sphere around an observation point, and the relevant ray directions are encoded into cotangent directions in terms of coefficients of Gaussian wave packet expansions. Because fast Gaussian wave packet transforms are discrete forms of the so-called Fourier–Bros–Iagolnitzer transform [13, 14] which is an ideal tool for carrying out microlocal and semiclassical analysis, it is natural for us to design NMLA based on fast Gaussian wave packet transforms so that we can localize both spatial locations by Gaussian windows in space and cotangent directions by Gaussian windows in frequency simultaneously.

Now, we discuss the accuracy and time complexity of the original NMLA [2, 5]. Let ω be the frequency parameter. Let $\widetilde{u}$ be a wavefield with reduced frequency $\widetilde{\omega} \sim \mathcal{O}(\omega^\alpha)$ with $0 < \alpha < 1$. In the original NMLA, to analyze the ray directions at a point $\mathbf{x}_0$ (we call this an observation point), Dirichlet or impedance observables are collected on a sphere with radius $r \sim \mathcal{O}(\omega^{-\beta})$, where β is a positive number. The number of observables is proportional to $\widetilde{\omega} r^{d-1} \sim \mathcal{O}(\omega^{(\alpha-\beta)(d-1)})$, where d is the spatial dimension. Then a linear filter is applied to the observables via fast Fourier transforms and the approximate directions are given by the location of peaks. Therefore, the time complexity of the original NMLA is $\mathcal{O}(\omega^{(\alpha-\beta)(d-1)} \log \omega)$ per observation point. In principle, the original NMLA performs uniform sampling of the directions on the unit sphere $\mathbb{S}^{d-1}$. Therefore, the best accuracy of directions that it can achieve is $\mathcal{O}(\omega^{(\beta-\alpha)})$. In [5], the analysis shows that when $\widetilde{u}$ is a superposition of plane waves up to a small perturbation, one can take $\beta = 0$ and achieve an accuracy of directions of $\mathcal{O}(\omega^{-\alpha})$. However, when $\widetilde{u}$ is a wavefield generated by a point source in a homogeneous medium, it requires $\beta \geq 0.5\alpha$ and the accuracy of directions degrades to $\mathcal{O}(\omega^{-0.5\alpha})$. To improve accuracy of directions, the authors in [5] propose a second-order-correction technique, which uses the curvature to update the filter and requires $\beta \geq 0.25\alpha$, and the resulting accuracy of directions degrades to $\mathcal{O}(\omega^{-0.75\alpha})$.

In our novel NMLA, we apply a d-dimensional fast Gaussian wave-packet transform (GWT) to uniformly spaced samples of $\widetilde{u}$ on a Cartesian grid. The wavefield $\widetilde{u}$ is then decomposed into a linear combination of Gaussian wave packets, which is locally approximated by

$$\widetilde{u}(\mathbf{x}) \approx \sum_{\mathbf{k} \approx \widetilde{\omega}/c(\mathbf{x}_0)} z(\mathbf{k}) e^{i\mathbf{k}\cdot(\mathbf{x}-\mathbf{x}_0)}$$

at an observation $\mathbf{x}_0$. To extract the dominant directions, essentially,[1] we apply a

---

[1]In practice, we don't compute $Z(\mathbf{d})$.

TABLE 1
Time complexity and accuracy of Algorithm 3.

d	α	β	Time complexity		Best accuracy
			Homogeneous Medium	Heterogeneous Medium	
2	0.5	0	$\omega^{0.5}\log\omega$	$\omega^{0.5}\log\omega$	$\omega^{-0.5}$
		0.25	$\omega^{0.25}\log\omega$	$\omega^{0.5}\log\omega$	$\omega^{-0.25}$
		0.50	$\omega^{0}\log\omega$	$\omega^{0}\log\omega$	ω^{0}
3		0	$\omega^{1}\log\omega$	$\omega^{1}\log\omega$	$\omega^{-0.5}$
		0.25	$\omega^{0.5}\log\omega$	$\omega^{0.75}\log\omega$	$\omega^{-0.25}$
		0.50	$\omega^{0}\log\omega$	$\omega^{0}\log\omega$	ω^{0}

peak-picking algorithm to the following discrete signal:

$$Z(\mathbf{d}) = \max_{\mathbf{k}/|\mathbf{k}|=\mathbf{d}} |z(\mathbf{k})|,$$

defined for some $\mathbf{d} \in \mathbb{S}^{d-1}$. Our NMLA has the following time complexity:

$$(1.1) \quad \begin{cases} \omega^{(\alpha-\beta)(d-1)}\log\omega & \text{when the medium is homogeneous,} \\ \omega^{\min\{(\alpha-\beta)(d-1)+\beta d,\,(\alpha-\beta)d\}}\log\omega & \text{otherwise,} \end{cases}$$

where β is specified later. Based on the number of samples of the directions in $\mathbb{S}^{d-1}$, we deduce that the best accuracy of the new NMLA is $\mathcal{O}(\omega^{\beta-\alpha})$. In Table 1, we show the time complexity per observation point and the highest accuracy of directions for $\alpha = 0.5$ with different choices of d and β. We can observe that, for homogeneous media, $\beta = 0$ or $\beta = \alpha$, the time complexity is the same as the original NMLA. In our numerical experiments, we take $\beta = 0$, $\alpha = 0.5$ or 0.25. The results show that the best accuracy is achievable for superposition of plane waves but degraded accuracy is also observed for spherical waves in homogeneous media.

1.1. The high-frequency Helmholtz problem. We consider the following model problem. Let $\omega > 0$ be the frequency and $\Omega \subset \mathbb{R}^d$ for $d = 2$ or 3. Find $u \in H^2(\Omega)$ such that

$$(1.2) \qquad\qquad -\nabla^2 u - (\omega/c)^2 u = f \quad \text{in } \Omega,$$

where we may impose impedance boundary conditions, Cauchy conditions, or perfectly matched layer(PML) boundary conditions. Here c is the wave speed, which is a smooth function with positive lower and upper bound, u is the wavefield, and $f \in L^2(\Omega)$ is the source function.

Solving the Helmholtz problem in the high-frequency regime (when ω is large) is a difficult task. First of all, the solution u becomes more oscillatory as ω gets larger. The Shannon sampling theorem implies that accurately representing u requires $\mathcal{O}(\omega^d)$ degrees of freedom. Nonetheless, accurately solving the Helmholtz equation by many typical methods (e.g., finite element methods with low-order polynomials) requires even more degrees of freedom asymptotically in that the ratio of the error of the numerical solution to the best approximation grows as ω gets larger; this phenomenon is usually called the pollution effect [15, 16].

To tackle the pollution effect, a popular strategy is to incorporate oscillatory behavior of the solution into the basis of a finite element method. The *phase-based*

methods [17, 18, 19] explicitly incorporate the phase functions into the basis. For a simple geometry and a homogeneous medium, one can compute the phase functions analytically, but it is difficult to do so in general. Another way is to compute the phase function numerically, for example, by solving the eikonal equation. We note that the viscosity solution of the eikonal equation is single valued and only represents the phase corresponding to the first-arrival time of wavefronts. This causes difficulties when a medium is heterogeneous, in which the number of wavefronts passing through a point varies depending on locations. The *ray-based methods* [6, 7, 8, 9] consider the local ray directions instead of the phase function. It is numerically shown that by incorporating dominant ray directions into the basis, the efficiency and accuracy of solving the Helmholtz equation in an inhomogeneous medium can be significantly improved. To find the local ray directions, one may use Lagrangian methods, such as ray tracing [9], wavefront reconstruction [8], or one may apply NMLA [2, 5] to a wavefield solution [6, 7].

1.2. Relation to Trefftz methods for the Helmholtz equation. In a recent survey [20], the authors have given a quite comprehensive review of construction and properties of Trefftz variational methods for the Helmholtz equation. Since such methods use oscillating basis functions in the trial spaces, they may achieve better approximation properties than classical piecewise polynomial spaces. So far, as stated in [20], it is hard to make unequivocal statements about the merits of *exact Trefftz* methods in that theory developed in the literature such as [21, 22, 23] fails to provide information about the crucial issue of ω-robust accuracy with ω-independent cost, and these methods provide no escape from the pollution error.

Since Trefftz finite element methods require test and trial functions to be exact local solutions of the Helmholtz equation, these methods are able to easily deal with discontinuous and piecewise constant wave speeds. However, when the wave speed is smoothly varying, in general, there are no exact analytical solutions for the underlying Helmholtz equation so that no analytical Trefftz functions are available either. Therefore, *approximate Trefftz* functions are appealing for problems with smoothly varying wave speeds; see [9] for ray-based modulated plane-wave discontinuous Galerkin methods and [24] for generalized plane-wave numerical methods, which are two examples of such approximate Trefftz methods.

As stated in [20], the policy of incorporating local direction of rays is particularly attractive for plane-wave based approximate Trefftz methods, since plane-wave basis functions naturally encode a direction of propagation, and overall accuracy may benefit significantly from a priori directional adaptivity [17, 18, 19]; moreover, the survey [20] also remarks that this strategy appears as the most promising way to achieve ω-uniform accuracy with numbers of degrees of freedom that remain ω-uniformly bounded or display only moderate growth as $\omega \to \infty$. On the one hand, the methods in [17, 19] are able to incorporate ray directions only when the underlying geometry is simple and the wave speed is constant, in which the resulting ray directions can be computed on the fly; on the other hand, the works in [9, 6, 7, 8] have developed such ray-based plane-wave methods for smoothly varying wave speeds, in which ray directions are obtained a priori in some ingenious ways. From this perspective, the method proposed in this article can be viewed as a plane-wave based approximate Trefftz method as well in that we develop a versatile approach to obtain ray directions from highly oscillatory wave fields by carrying out NMLA via fast GWTs [3, 4] and further incorporate these directions into an inter-penalty discontinuous Galerkin (IPDG) method.

1.3. Geometric optics and probing. In this section, we describe the idea of "probing" from [6] for solving the high-frequency Helmholtz problem. We use the notation $f(x) \lesssim g(x)$ to denote that there is a positive constant C which is independent of ω such that $|f(x)| \leq C|g(x)|$. We start by studying the geometric optics. Let $\mathbf{x} \in \Omega$. We consider the following geometric optics ansatz (cf. [25, 26, 27, 28]) for the Helmholtz equation:

$$u(\mathbf{x}) = \text{ superposition of } \left\{ A_n(\mathbf{x}) e^{i\omega\phi_n(\mathbf{x})} \right\}_{n=1}^{N(\mathbf{x})} + \mathcal{O}(\omega^{-1}),$$

where $N(\mathbf{x})$ is the number of wavefronts passing through $\mathbf{x}$, and A_n and ϕ_n are the amplitude and phase functions, respectively. We assume that A_n and ϕ_n are independent of the frequency ω, but they depend on the wave speed $c(\mathbf{x})$ and the source $f(\mathbf{x})$. Fix $\mathbf{x}_0 \in \Omega$ and consider the Taylor expansion of each ϕ_n for $|\mathbf{x} - \mathbf{x}_0| < h \ll 1$, so that we have

$$\phi_n(\mathbf{x}) = \phi_n(\mathbf{x}_0) + |\nabla\phi_n(\mathbf{x}_0)| \, \mathbf{d}_n \cdot (\mathbf{x} - \mathbf{x}_0) + \mathcal{O}(h^2),$$

where $\mathbf{d}_n := \frac{\nabla\phi_n(\mathbf{x}_0)}{|\phi_n(\mathbf{x}_0)|}$ is the ray direction. Similarly, the Taylor expansion of A_n gives

$$A_n(\mathbf{x}) = A_n(\mathbf{x}_0) + \nabla A_n(\mathbf{x}_0) \cdot (\mathbf{x} - \mathbf{x}_0) + \mathcal{O}(h^2).$$

Note that $c(\mathbf{x})|\nabla\phi_n(\mathbf{x})|$ is a constant for each wave component. Without loss of generality, we may assume this constant to be 1 for every wave component. Hence, each wave component in the solution $u(\mathbf{x})$ can be written as

$$A_n(\mathbf{x}) e^{i\omega\phi_n(\mathbf{x})} = B_n(\mathbf{x} - \mathbf{x}_0) e^{i(\omega/c(\mathbf{x}_0)) \, \mathbf{d}_n \cdot (\mathbf{x} - \mathbf{x}_0)} + \mathcal{O}(h^2 + \omega h^2 + \omega^{-1}),$$

where $B_n(\mathbf{x}) = e^{i\omega\phi_n(\mathbf{x}_0)}(A(\mathbf{x}_0) + \nabla A_n(\mathbf{x}_0) \cdot \mathbf{x})$ is a linear function. By taking $h \sim \mathcal{O}(\omega^{-1})$, we see that $u(\mathbf{x})$ can be approximated by superposition of products of a linear function and a plane wave with an error of $\mathcal{O}(\omega^{-1})$. This motivates us to use products of bilinear functions with $e^{i(\omega/c(\mathbf{x}_0)) \, \mathbf{d}_n \cdot (\mathbf{x} - \mathbf{x}_0)}$ as the local basis.

Let $\widetilde{u}$ be the solution to the Helmholtz equation (1.2) with the same source $f(\mathbf{x})$ and wave speed $c(\mathbf{x})$ but a reduced frequency $\widetilde{\omega} \sim \mathcal{O}(\omega^\alpha)$. We can solve $\widetilde{u}$ numerically using appropriate source functions and boundary conditions and then apply NMLA to extract the directions from the numerical solution. A recent preasymptotic analysis for standard finite element methods [29] implies that for $0 < \alpha < 1/2$, solving the Helmholtz equation (1.2) in a homogeneous medium by a standard finite element method with bilinear basis with mesh size $\mathcal{O}(\omega^{-1})$ gives a convergence of order $\mathcal{O}(\omega^{2\alpha-2})$ as $\omega \to \infty$. This suggests that we can extract accurate directions from the numerical solution of $\widetilde{u}$ produced by a standard finite element method.

In this paper, we use an IPDG method with bilinear basis to solve for $\widetilde{u}$ on a mesh with mesh size $\widetilde{h} \sim \mathcal{O}(\omega^{-1})$. Then we apply our NMLA to extract the directions at the tile centers of a mesh with mesh size $h \sim O(\omega^{-1})$, where the mesh size h and $\widetilde{h}$ could be different. Using these meshes and directions, we form another IPDG system with the local basis consisting of products of bilinear functions and plane waves. This IPDG system is shown to have second-order convergence for fixed frequency ω as mesh size $h \to 0$ and no pollution effect in the numerical experiments [18].

This paper is organized as follows. In section 2, we briefly describe the ray-based IPDG method with various boundary conditions, and the approximation properties of the underlying finite element spaces. In section 3, we discuss the novel NMLA

in detail. In section 4, we provide various numerical experiments and the results to demonstrate the performance of the novel NMLA.

2. The ray-based IPDG method.

2.1. Finite element spaces and formulation. For simplicity, in this section we consider the domain of interest to be $\Omega = [0,1]^d$. Let M be the number of tiles per dimension. We partition Ω into M^d d-dimensional cubic tiles

$$K_{\mathbf{j}} := [j_1/M, (j_1+1)/M] \times \cdots \times [j_d/M, (j_d+1)/M]$$

for $\mathbf{j} = (j_1, \ldots, j_d) \in \mathbb{Z}_M^d$. Let $\mathcal{T}_h$ be the set of all these tiles and $\mathbf{x}_K$ be the center of tile K for each $K \in \mathcal{T}_h$. Also, we define $\mathcal{F}_h$, $\mathcal{F}_h^I$, and $\mathcal{F}_h^B$ to be the set of all faces, interior faces, and boundary faces of the tiles, respectively.

Next, we describe the finite element space. Fix $K \in \mathcal{T}_h$. There are 2^d standard Lagrange-type bilinear basis functions on K. Let $\mathbf{x}_{i,K}$ be the vertices of K and $\varphi_{j,K}$ be the standard Lagrange-type bilinear basis on K such that $\varphi_{j,K}(\mathbf{x}_{i,K}) = \delta_{ij}$. Given a set of directions Θ_K for K, we define the basis functions by

$$\varphi_{j,K}(\mathbf{x})e^{i(\omega/c(\mathbf{x}_K))\,\mathbf{d}\cdot(\mathbf{x}-\mathbf{x}_K)}, \quad \mathbf{d} \in \Theta_K, 1 \le j \le 2^d.$$

Then we denote the local approximation space by $V_h(\Theta_K)$ which consists of linear combinations of these basis functions over $\mathbb{C}$ and the global approximation space by

$$V_h = \Pi_{K \in \mathcal{T}_h} V_h(\Theta_K).$$

Next, we discuss the IPDG formulation for the Helmholtz equation with different boundary conditions.

2.1.1. Impedance boundary condition. Consider the Helmholtz problem (1.2) with an impedance boundary condition

$$\nabla u \cdot n + i(\omega/c)u = g \quad \text{on } \partial\Omega.$$

Following the derivation of the standard IPDG method [30], we obtain the following scheme for this problem: Find $u_h \in V_h$ such that for any $v_h \in V_h$,

$$a_h(u_h, v_h) - \omega^2(c^{-2}u_h, v_h)_{L^2(\Omega)} = (f, v_h)_{L^2(\Omega)} + (g, v_h)_{L^2(\partial\Omega)},$$

where a_h is given by

$$a_h(u,v) := \int_\Omega \nabla u \cdot \nabla \overline{v}\, dx - \int_{\mathcal{F}_h^I} \{\!\{\nabla u\}\!\} \cdot [\![\overline{v}]\!]\, ds$$

$$- \int_{F_h^I} [\![u]\!] \cdot \{\!\{\nabla \overline{v}\}\!\}\, ds + \frac{\mathbf{a}}{h} \int_{\mathcal{F}_h^I} [\![u]\!] \cdot [\![\overline{v}]\!]\, ds + i \int_{\mathcal{F}_h^B} \kappa u \overline{v}\, ds$$

with $\mathbf{a}$ serving as the penalty parameter. Here we have used the usual average and jump operators for discontinuous Galerkin methods. Let $K^\pm \in \mathcal{T}_h$ be two tiles sharing an edge $F \in \mathcal{F}_h$, and $\mathbf{n}^\pm$ be the outward normal of K, which is perpendicular to F. Let u be a smooth scalar function defined on $K^\pm$. Then,

$$\{\!\{\nabla u\}\!\} := \frac{1}{2}(\nabla u^+ + \nabla u^-), \quad [\![u]\!] := u^+\mathbf{n}^+ + u^-\mathbf{n}^-.$$

2.1.2. Cauchy boundary condition. Consider the Helmholtz problem (1.2) with the Cauchy boundary condition:

$$u = g_1 \text{ and } \nabla u \cdot \mathbf{n} = g_2 \quad \text{on } \partial \Omega.$$

We define the interior local approximation space

$$V_h^\circ(\Theta_K) := \text{ span} \left\{ \varphi_{j,K}(\mathbf{x}) e^{i\omega \mathbf{d} \cdot (\mathbf{x} - \mathbf{x}_K)} : \mathbf{d} \in \Theta_K, \varphi_j|_{\partial\Omega} \neq 0, 1 \le j \le N_b \right\},$$

and the interior global approximation space $V_h^\circ := \Pi_{K \in \widetilde{\mathcal{T}}_h} V_h^\circ(\Theta_K)$. Then we solve the following problem: Find $u_h \in V_h(\Theta_K)$ such that for any $v_h \in V_h$,

$$a_h^C(u_h, v_h) - \omega^2(c^{-2}u_h, v_h)_{L^2(\Omega)} = (f, v_h)_{L^2(\Omega)} \quad \text{for any } v_h \in V_h^\circ,$$

$$\int_{\partial\Omega} u_h v_h \, ds = \int_{\partial\Omega} g_1 v_h \, ds \quad \text{for any } v_h \in V_h \setminus V_h^\circ,$$

$$\int_{\partial\Omega} \nabla u_h \cdot \mathbf{n} \, v_h \, ds = \int_{\partial\Omega} g_2 v_h \, ds \quad \text{for any } v_h \in V_h \setminus V_h^\circ,$$

where a_h^C is given by

$$a_h^C(u, v) := \int_\Omega \nabla u \cdot \nabla \overline{v} \, dx - \int_{\mathcal{F}_h^I} \{\!\!\{\nabla u\}\!\!\} \cdot [\![\overline{v}]\!] \, ds$$

$$- \int_{\mathcal{F}_h^I} [\![u]\!] \cdot \{\!\!\{\nabla \overline{v}\}\!\!\} \, ds + \frac{\mathbf{a}}{h} \int_{\mathcal{F}_h^I} [\![u]\!] \cdot [\![\overline{v}]\!] \, ds.$$

2.1.3. Perfectly matched layer. Suppose that Ω is embedded in a larger domain $\widetilde{\Omega} := [-\delta, 1 + \delta]^d$, where $\delta > 0$ is the width of the PMLs. Typically, we choose δ to be approximately several wavelengths. Further assume that δ is divisible by the mesh size h. In this way, we can divide $\widetilde{\Omega}$ into $(M + 2\delta/h)^d$ cubic tiles. Denote the set of all these tiles by $\widetilde{\mathcal{T}}_h$. Note that $\mathcal{T}_h \subset \widetilde{\mathcal{T}}_h$. By abuse of notation, we denote the tiles in $\widetilde{\mathcal{T}}_h$ by $K_{\mathbf{j}} = [\frac{j_1}{M}, \frac{j_1+1}{M}] \times \cdots \times [\frac{j_d}{M}, \frac{j_d+1}{M}]$ for $\mathbf{j} \in \mathbb{Z}_{M+2\delta/h}^d$. Supposing that Θ_K is defined for all $K_{\mathbf{j}} \in \widetilde{\mathcal{T}}_h$, we extend the definition of the interior local approximation space $V^\circ(\Theta_K)$ and the interior global approximation space V° to the mesh $\widetilde{\mathcal{T}}_h$. We denote the extended spaces by $\widetilde{V}^\circ(\Theta_K)$ and $\widetilde{V}^\circ$, respectively. Then we introduce the PML function $s(x)$:

$$s(x) := \frac{1}{1 + \sigma(x)/x}, \quad \sigma(x) := \frac{A_{pml}}{\delta^2} \left((x - \delta)^2 \chi_{\{x < \delta\}}(x) + (x - 1 - \delta)^2 \chi_{\{x > 1 + \delta\}} \right),$$

where χ_S is the characteristic function of set S, A_{pml} controls the magnitude of $s(x)$, and δ is the width of the PML. Define

$$\widetilde{\nabla} := \left(s(x_1) \frac{\partial}{\partial x_1}, \dots, s(x_d) \frac{\partial}{\partial x_d} \right).$$

The IPDG scheme for the Helmholtz problem with PML boundary conditions is find $u_h \in \widetilde{V}_h^\circ$ such that

$$\widetilde{a}_h(u_h, v_h) - \omega^2(c^{-2}u_h, v_h)_{L^2(\Omega)} = (f, v_h)_{L^2(\Omega)} \text{ for any } v_h \in \widetilde{V}_h^\circ,$$

where

$$\widetilde{a}_h(u,v) := \int_\Omega \widetilde{\nabla} u \cdot \widetilde{\nabla} \overline{v}\, dx - \int_{\mathcal{F}_h^I} \{\{\widetilde{\nabla} u\}\} \cdot [[\overline{v}]]\, ds$$

$$- \int_{\mathcal{F}_h^I} [[u]] \cdot \{\{\widetilde{\nabla}\overline{v}\}\}\, ds + \frac{\mathbf{a}}{h} \int_{\mathcal{F}_h^I} [[u]] \cdot [[\overline{v}]]\, ds.$$

2.2. Approximation properties of the ray-based IPDG method. In this section, we estimate the approximation error of the solution u by the global approximation space V_h. Consider $u(\mathbf{x}) = A(\mathbf{x})e^{i\omega\phi(\mathbf{x})} + \mathcal{O}(\omega^{-1})$ for $\mathbf{x} \in \Omega$ with $u \in L^2(\Omega), A \in H^2(\Omega)$, and $\phi \in H^2(\Omega)$. Let $K \in \mathcal{T}_h$. Assume that $\mathbf{d_K} := \nabla\phi(\mathbf{x}_K)/|\nabla\phi(\mathbf{x}_K)|$ is the direction of u at $\mathbf{x}_K$. Suppose the set of approximate directions $\Theta_K = \{\widehat{\mathbf{d}}_K\}$ incurs a small error ε, i.e., $\sup_{K\in\mathcal{T}_h} \left|\widehat{\mathbf{d}}_K - \mathbf{d}_K\right| < \varepsilon$. Define the nodal interpolation of u on K by

$$u_I(\mathbf{x}) := \sum_{j=1}^{N_b} A(\mathbf{x}_{j,K})\varphi_j(\mathbf{x})e^{i\omega\widehat{\phi}(\mathbf{x})}, \quad \widehat{\phi}(\mathbf{x}) := \phi(\mathbf{x}_K) + |\nabla\phi(\mathbf{x}_K)|\widehat{\mathbf{d}} \cdot (\mathbf{x} - \mathbf{x}_K),$$

where $\mathbf{x}_{j,K}$ are the vertices of K. Then,

$$\left\|\phi(\mathbf{x}) - \widehat{\phi}(\mathbf{x})\right\|_{L^2(K)} \leq \|\phi(\mathbf{x}) - \phi(\mathbf{x}_K) - \nabla\phi(\mathbf{x}_K) \cdot (\mathbf{x} - \mathbf{x}_K)\|_{L^2(K)}$$

$$+ |\nabla\phi(\mathbf{x}_K)| \left\|(\mathbf{d}_K - \widehat{\mathbf{d}}_K) \cdot (\mathbf{x} - \mathbf{x}_K)\right\|_{L^2(K)}$$

$$\lesssim h^2 \left\|\nabla^2\phi\right\|_{L^\infty(K)} |K| + \varepsilon h |\nabla\phi(\mathbf{x}_K)| \, |K|.$$

Using the triangle inequality and smoothness of u,

$$\|u(\mathbf{x}) - u_I(\mathbf{x})\|_{L^2(K)}$$

$$\leq \left\|A(\mathbf{x})e^{i\omega\phi(\mathbf{x})} - \sum_{j=1}^{N_b} A(\mathbf{x}_{j,K})\varphi_j(\mathbf{x})e^{i\omega\phi(\mathbf{x})}\right\|_{L^2(K)}$$

$$+ \left\|\sum_{j=1}^{N_b} A(\mathbf{x}_{j,K})\varphi_j(\mathbf{x})\left[e^{i\omega\phi(\mathbf{x})} - e^{i\omega\widehat{\phi}(\mathbf{x})}\right]\right\|_{L^2(K)} + \mathcal{O}(\omega^{-1})$$

$$\leq \left\|A(\mathbf{x}) - \sum_{j=1}^{N_b} A(\mathbf{x}_{j,K})\varphi_j(\mathbf{x})\right\|_{L^2(K)}$$

$$+ \sum_{j=1}^{N_b} \|A\|_{L^\infty(\Omega)} \left\|e^{i\omega\phi(\mathbf{x})} - e^{i\omega\widehat{\phi}(\mathbf{x})}\right\|_{L^2(K)} + \mathcal{O}(\omega^{-1})$$

$$\lesssim h^2 |A|_{H^2(K)} + \omega \|A\|_{L^\infty(\Omega)} \left\|\phi(\mathbf{x}) - \widehat{\phi}(\mathbf{x})\right\|_{L^2(K)} + \omega^{-1}$$

$$\lesssim h^2 |A|_{H^2(K)} + \omega \|A\|_{L^\infty(\Omega)} \left(h^2 \left\|\nabla^2\phi\right\|_{L^\infty(\Omega)} + \varepsilon h |\nabla\phi(\mathbf{x}_K)|\right) |K| + \omega^{-1}.$$

Summing this inequality for each $K \in \mathcal{T}_h$,

$$\|u(\mathbf{x}) - u_I(\mathbf{x})\|_{L^2(\Omega)} \lesssim h^2 |A|_{H^2(\Omega)} + \omega \|A\|_{L^\infty(\Omega)} \left(h^2 \left\|\nabla^2\phi\right\|_{L^\infty(\Omega)}\right.$$

$$\left.+ \varepsilon h \sup_{K\in\mathcal{T}_h} |\nabla\phi(\mathbf{x}_K)|\right) + \omega^{-1}$$

$$\lesssim h^2 + \omega h^2 + \omega\varepsilon h + \omega^{-1}.$$

Supposing that the mesh size $h \sim \mathcal{O}(\omega^{-1})$ and $\omega^{-1} \lesssim \varepsilon$, we have

$$\|u(\mathbf{x}) - u_I(\mathbf{x})\|_{L^2(\Omega)} \lesssim \varepsilon.$$

Hence, when $\sup_{K \in \mathcal{T}_h} \inf_{\widehat{\mathbf{d}}_K \in \Theta_K} \left|\mathbf{d}_K - \widehat{\mathbf{d}}_K\right| \lesssim \omega^{-\gamma}$ for some $0 < \gamma < 1$,

$$\inf_{u_h \in V_h} \|u(\mathbf{x}) - u_h(\mathbf{x})\|_{L^2(\Omega)} \leq \|u(\mathbf{x}) - u_I(\mathbf{x})\|_{L^2(\Omega)} \lesssim \omega^{-\gamma}.$$

To conclude, when the approximate direction has an accuracy of $\mathcal{O}(\omega^{-\gamma})$, the least approximation error of u on V_h is also $O(\omega^{-\gamma})$.

We note that the analysis in [6, 7] is different from the above analysis, as the basis functions are different. In [6, 7], the basis functions are continuous across the boundary of each tile, where each of the basis functions is a product of a polynomial nodal basis with a wave function that corresponds to a direction *defined at that nodal point*. In contrast, the IPDG method we use does not enforce the continuity of the basis functions across the boundary of each tile, where each of the basis functions is a product of a bilinear basis defined on a tile with a wave function that corresponds to a direction *defined on that tile*.

3. NMLA by fast GWTs.

3.1. The fast GWT. We will carry out NMLA by using the fast GWT developed in [3]. For simplicity, we define the discrete GWT for periodic signals in the domain $[0, 1]^d$. Let N be the number of samples of the signal in each dimension. We define the spatial domain X and the frequency domain Y by

$$X := \left\{(n_1/N, \ldots, n_d/N) : n_1, \ldots, n_d \in \mathbb{Z} \cap [0, N)\right\},$$
$$Y := \left\{(k_1, \ldots, k_d) : k_1, \ldots, k_d \in \mathbb{Z} \cap [-N/2, N/2)\right\}.$$

We define the forward discrete Fourier transform and its inverse on X and Y by

$$\widehat{f}_1(\boldsymbol{\xi}) := \frac{1}{N^{d/2}} \sum_{\mathbf{x} \in X} e^{-2\pi i \mathbf{x} \cdot \boldsymbol{\xi}} f_1(\mathbf{x}), \quad \boldsymbol{\xi} \in Y,$$
$$f_2(\mathbf{x}) := \frac{1}{N^{d/2}} \sum_{\boldsymbol{\xi} \in Y} e^{2\pi i \mathbf{x} \cdot \boldsymbol{\xi}} \widehat{f}_2(\boldsymbol{\xi}), \quad \mathbf{x} \in X,$$

for any signal f_1 defined on X and $\widehat{f}_2$ defined on Y.

Let W be an integer such that W divides N. We partition the frequency domain Y into d-dimensional cubes of size W in each dimension, as illustrated in Figure 1. We index these cubes by $\mathbf{i} \in \mathbb{Z}_{N/W}^d$, and denote the cubes by $B_{\mathbf{i}}$. We call each $B_{\mathbf{i}}$ a block and W the block size. We denote the center of $B_{\mathbf{i}}$ by $\boldsymbol{\xi}_{\mathbf{i}}$ and the set of all these centers by Ξ. Define $\widetilde{B}_{\mathbf{i}} := \Pi_{s=1}^d [\xi_s - W, \xi_s + W]$, periodically, for $\boldsymbol{\xi}_{\mathbf{i}} = (\xi_1, \ldots, \xi_d)$, and let $\chi_{\mathbf{i}}(\boldsymbol{\xi})$ be the characteristic function of the set $\widetilde{B}_{\mathbf{i}}$. Then we associate each $B_{\mathbf{i}}$ with a window function

$$g_{\mathbf{i}}(\boldsymbol{\xi}) = e^{-|\boldsymbol{\xi} - \boldsymbol{\xi}_{\mathbf{i}}|^2/\sigma^2} \chi_{\mathbf{i}}(\boldsymbol{\xi}), \quad \boldsymbol{\xi} \in Y,$$

which is compactly supported on $\widetilde{B}_{\mathbf{i}}$. We note that the width of each $\widetilde{B}_{\mathbf{i}}$ is $L := 2W$ and these cubes overlap. We choose $\sigma = W/2$ in the definition of $g_{\mathbf{i}}$ to ensure that
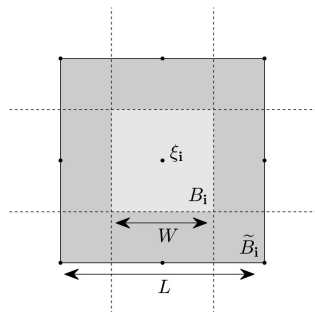
FIG. 1. *The geometries of the blocks $B_{\mathbf{i}}$ in two dimensions. The dots represent the block centers and the dashed lines are the interfaces between the blocks. The solid rectangle is the extended block $\widetilde{B}_{\mathbf{i}}$, which is the support of $g_{\mathbf{i}}$.*

the difference between $g_{\mathbf{i}}$ and the Gaussian function is small outside $\widetilde{B}_{\mathbf{i}}$. Define

$$h_{\mathbf{i}}(\boldsymbol{\xi}) := \frac{g_{\mathbf{i}}(\boldsymbol{\xi})}{\sum_{\mathbf{i}}(g_{\mathbf{i}}(\boldsymbol{\xi}))^2}, \quad \boldsymbol{\xi} \in Y,$$

which has the same support as $g_{\mathbf{i}}$. Then the product of $h_{\mathbf{i}}$ and $g_{\mathbf{i}}$ forms a partition of unity, i.e.,

$$\sum_{\mathbf{i}} h_{\mathbf{i}}(\boldsymbol{\xi})g_{\mathbf{i}}(\boldsymbol{\xi}) = 1.$$

For any $\mathbf{i} \in \mathbb{Z}_{N/W}^d, \mathbf{k} \in \mathbb{Z}_L^d$, we define the functions $\phi_{\mathbf{i},\mathbf{k}}$ and $\psi_{\mathbf{i},\mathbf{k}}$ in the frequency domain Y:

$$\hat{\phi}_{\mathbf{i},\mathbf{k}}(\boldsymbol{\xi}) := \frac{1}{L^{d/2}}e^{-2\pi i \mathbf{k}\cdot\boldsymbol{\xi}/L}g_{\mathbf{i}}(\boldsymbol{\xi}), \quad \hat{\psi}_{\mathbf{i},\mathbf{k}}(\boldsymbol{\xi}) := \frac{1}{L^{d/2}}e^{-2\pi i \mathbf{k}\cdot\boldsymbol{\xi}/L}h_{\mathbf{i}}(\boldsymbol{\xi}) \quad \forall \boldsymbol{\xi} \in Y.$$

By applying the inverse discrete Fourier transform, we see that in the spatial domain $\phi_{\mathbf{i},\mathbf{k}}$ is approximately a product of a plane wave and a Gaussian window centered at $\mathbf{x} = \mathbf{k}/L$:

$$(3.1) \qquad \phi_{\mathbf{i},\mathbf{k}}(\mathbf{x}) \approx \left(\sqrt{\frac{\pi}{NL}}\sigma\right)^d e^{2\pi i \left(\mathbf{x}-\frac{\mathbf{k}}{L}\right)\cdot\boldsymbol{\xi}_{\mathbf{i}}} e^{-\sigma^2\pi^2\left|\mathbf{x}-\frac{\mathbf{k}}{L}\right|^2} \quad \forall \mathbf{x} \in X.$$

Besides, for any L^2-function f defined on X, we can represent f by $\phi_{\mathbf{i},\mathbf{k}}$:

$$f(\mathbf{x}) = \sum_{\mathbf{i},\mathbf{k}\in\mathbb{Z}_N^d} z_{\mathbf{i},\mathbf{k}}\,\phi_{\mathbf{i},\mathbf{k}}(\mathbf{x}), \qquad z_{\mathbf{i},\mathbf{k}} = \langle\psi_{\mathbf{i},\mathbf{k}}, f\rangle = \sum_{\mathbf{x}\in X} \psi_{\mathbf{i},\mathbf{k}}(\mathbf{x})f(\mathbf{x}).$$

To compute $z_{\mathbf{i},\mathbf{k}}$, we observe that

$$z_{\mathbf{i},\mathbf{k}} = \langle\psi_{\mathbf{i},\mathbf{k}}, f\rangle = \langle\hat{f}, \hat{\psi}_{\mathbf{i},\mathbf{k}}\rangle = \sum_{\boldsymbol{\xi}\in Y} \frac{1}{L^{d/2}}e^{2\pi i \frac{\mathbf{k}\cdot\boldsymbol{\xi}}{L}}h_{\mathbf{i}}(\boldsymbol{\xi})\hat{f}(\boldsymbol{\xi}),$$

where the summation is indeed a d-dimensional inverse Fourier transform of size L. To see this clearly, we introduce a new function $t(\boldsymbol{\eta}) := h_{\mathbf{i}}(\boldsymbol{\xi})\hat{f}(\boldsymbol{\xi})$, $\boldsymbol{\eta} \in \mathbb{Z}_L^d$, where

$\boldsymbol{\xi} \equiv \boldsymbol{\eta}$ mod L. Then we can write

$$z_{\mathbf{i},\mathbf{k}} = \sum_{\boldsymbol{\eta} \in \mathbb{Z}_L^d} \frac{1}{L^{d/2}} e^{2\pi i \frac{\mathbf{k} \cdot \boldsymbol{\eta}}{L}} t(\boldsymbol{\eta}).$$

The process of computing $z_{\mathbf{i},\mathbf{k}}$ is called the *forward discrete GWT*.

We summarize the forward discrete GWT in Algorithm 1. Suppose $N \sim \mathcal{O}(\omega)$. In Algorithm 1, the time complexity of line 1 is $\mathcal{O}(\omega^d \log \omega)$. The number of iterations of the loop (lines 2–6) is $(N/W)^d$ and the slowest line in the loop is line 6, whose time complexity is $\mathcal{O}(W^d \log W)$. Hence the time complexity of Algorithm 1 is $\mathcal{O}(\omega^d \log \omega)$ for any choice of W.

Algorithm 1 Discrete GWT.

Input: f: signal defined on X; N: the size of X in each dimension; W: the blocksize.
Output: $z_{\mathbf{i},\mathbf{k}}$: the coefficients.
 1: $\hat{f} \leftarrow d$-dimensional forward FFT of f.
 2: **for** each $\mathbf{i} \in \mathbb{Z}_{N/W}^d$ **do**
 3:     Compute $h_{\mathbf{i}}(\boldsymbol{\xi}) \hat{f}(\boldsymbol{\xi})$ on $\widetilde{B}_{\mathbf{i}}$.
 4:     Compute $t(\boldsymbol{\eta}) = h_{\mathbf{i}}(\boldsymbol{\xi}) \hat{f}(\boldsymbol{\xi}), \boldsymbol{\eta} \equiv \boldsymbol{\xi} \mod L$.
 5:     $z_{\mathbf{i},\mathbf{k}} \leftarrow d$-dimensional inverse FFT of $t(\boldsymbol{\eta})$ of size L.
 6: **end for**

3.2. Learning wave directions via GWT. In this section, we consider the exact solution $\widetilde{u}$ with frequency $\widetilde{\omega} \sim \mathcal{O}(\omega^\alpha), 0 < \alpha \leq 1$, to the Helmholtz equation (1.2). We assume that $\widetilde{u}$ is periodic. To find the wave directions, we apply the forward discrete GWT to $\widetilde{u}$ with the number of samples in each dimension $N \sim \mathcal{O}(\omega^\alpha)$ and block size $W \sim \mathcal{O}(\omega^\beta)$, where W divides N and $\alpha > \beta$. As we have shown in (3.1), each $\phi_{\mathbf{i},\mathbf{k}}$ is approximately the product of a Gaussian function and a plane wave $e^{2\pi i \boldsymbol{\xi}_{\mathbf{i}} \cdot (\mathbf{x} - \mathbf{k}/L)}$, where each $\boldsymbol{\xi}_{\mathbf{i}} \in \Xi$ is the center of a d-dimensional cube $B_{\mathbf{i}}$ in the frequency domain. It suggests that by applying Algorithm 1, we can approximate directions of u at the points $\mathbf{x} = \mathbf{k}/L, \mathbf{k} \in \mathbb{Z}_L^d$.

Let $\mathbf{y} \in [-N/2, N/2)^d$ be arbitrary. Note that $\{B_{\mathbf{i}}\}$ is a partition of the frequency grid Y and Ξ is the set of centers of $\{B_{\mathbf{i}}\}$. We have

$$\inf_{\boldsymbol{\xi} \in \Xi} |\mathbf{y} - \boldsymbol{\xi}| \lesssim \mathcal{O}(\omega^\beta).$$

Let $\mathbf{d}$ be a direction of $\widetilde{u}$ at $\mathbf{x}_0 \in X$. There is an $\boldsymbol{\xi} \in \Xi$ such that

$$(3.2) \qquad \left| 2\pi \boldsymbol{\xi} - \widetilde{\omega} |\nabla \phi_n(\mathbf{x}_0)| \, \mathbf{d} \right| \lesssim \mathcal{O}(\omega^\beta).$$

Since $|\nabla \phi_n| \sim \mathcal{O}(1)$ for such $\boldsymbol{\xi}$, we have

$$\left| \frac{\boldsymbol{\xi}}{|\boldsymbol{\xi}|} - \mathbf{d} \right| \leq \left| \frac{\boldsymbol{\xi}}{|\boldsymbol{\xi}|} - \frac{2\pi \boldsymbol{\xi}}{\widetilde{\omega} |\nabla \phi_n|} \right| + \left| \frac{2\pi \boldsymbol{\xi}}{\widetilde{\omega} |\nabla \phi_n|} - \mathbf{d} \right| = \left| \frac{\boldsymbol{\xi}}{|\boldsymbol{\xi}|} \left(\frac{\widetilde{\omega} |\nabla \phi_n| - 2\pi |\boldsymbol{\xi}|}{\widetilde{\omega} |\nabla \phi_n|} \right) \right| + \left| \frac{2\pi \boldsymbol{\xi} - \widetilde{\omega} |\nabla \phi_n| \mathbf{d}}{\widetilde{\omega} |\nabla \phi_n|} \right|$$

$$\leq 2 \left| \frac{2\pi |\boldsymbol{\xi}| - \widetilde{\omega} |\nabla \phi_n|}{\widetilde{\omega} |\nabla \phi_n|} \right| \lesssim \mathcal{O}(\omega^{\beta - \alpha}).$$

In other words, the least approximation error to $\mathbf{d}$ by the direction of $\boldsymbol{\xi} \in \Xi$ is given by

$$\inf_{\boldsymbol{\xi} \in \Xi} \left| \frac{\boldsymbol{\xi}}{|\boldsymbol{\xi}|} - \mathbf{d} \right| \lesssim \mathcal{O}(\omega^{\beta - \alpha}).$$

Heuristically, the directions of $\boldsymbol{\xi}$ corresponding to the coefficients $z_{\mathbf{i},\mathbf{k}} \in \Xi_{\widetilde{\omega},c}$ with significant magnitudes are close to the true direction of $\widetilde{u}$. In the following discussion, we assume that these directions achieve the optimal accuracy. In order to measure the significance of $|z_{\mathbf{i},\mathbf{k}}|$, one may use the following absolute threshold to pick the directions at an observation point $\mathbf{x}_0 = \mathbf{k}/L$:

$$\Theta_{\mathbf{k},\delta} := \{\boldsymbol{\xi}/|\boldsymbol{\xi}| : |z_{\mathbf{i},\mathbf{k}}| > \delta\}.$$

One drawback of such a measure is that the number of directions in $\Theta_{\mathbf{k},\delta}$ depends on the strength of the signal near the observation point $\mathbf{x}_0$. As the strength of signal varies, such a measure is not applicable to, for example, wavefields in an absorbing medium. Instead, we propose a relative threshold to pick the directions as follows. For each observation point, we sort the corresponding $\{z_{\mathbf{i},\mathbf{k}}\}$ ($\mathbf{k}$ is fixed) in descending order by magnitude. Denote the sorted coefficients by $\{z_{j,\mathbf{k}}^{\leftarrow}\}$ and the corresponding block centers by $\{\boldsymbol{\xi}_j\}$. Then we take

$$(3.3) \qquad \Theta_{\mathbf{k},\eta} := \left\{ \frac{\boldsymbol{\xi}_j}{|\boldsymbol{\xi}_j|}, j \leq m^*(\eta) \right\}, \quad m^*(\eta) := \arg\min_m \frac{\sum_{j \leq m} \left|z_{j,\mathbf{k}}^{\leftarrow}\right|^2}{\sum_{\mathbf{i}} |z_{\mathbf{i},\mathbf{k}}|^2} > 1 - \eta,$$

where η controls the number of directions. In general, when η is larger, the size of $\Theta_{\mathbf{k},\eta}$ is smaller.

As we will see in the numerical experiments, usually in a neighborhood of each true direction of $\widetilde{u}$, there are a number of directions in $\Theta_{\mathbf{k},\eta}$ with coefficients of significant magnitude. In order to incorporate effective directions in $\Theta_{\mathbf{k},\eta}$ into a finite element scheme, we have to eliminate the redundancy and also cap the number of directions to avoid numerical instability in the linear system. We introduce two parameters, one being ε, the minimum distance between approximate directions, and the other being N_d, the maximum number of approximate directions. In Algorithm 2, we use these two parameters to select a subset of $\Theta_{\mathbf{k},\eta}$, which does not include any nearly linearly dependent directions. We note that when $\varepsilon = 0, N_d = \infty$, the approximate directions obtained from Algorithm 2 are exactly given by (3.3). By abuse of notation, we also denote this set by $\Theta_{\mathbf{k},\eta}$ and the parameters ε and N_d will be specified when necessary. We always assume that ε and N_d are independent of ω.

In Algorithm 2, we essentially apply a simple clustering procedure to determine the ray directions. It starts by picking the direction corresponding to the coefficient with the largest magnitude. Then it updates the measure of significance for all directions with distance less than ε to the picked direction. Next, it eliminates those directions from future consideration. And then it repeats, until no more directions with nonzero coefficients are available or N_d directions are already picked.

To see the time complexity of Algorithm 2, we consider $\eta = 0$ and $N_d = \infty$. Let $N_\xi := |\Xi|$. Note that on line 10, we set some of the $\{z_{\mathbf{i},\mathbf{k}}\}$ to zero, where the number of these $\{z_{\mathbf{i},\mathbf{k}}\}$ is the size of S. Also, the loop on lines 3–12 breaks after all $z_{\mathbf{i},\mathbf{k}}$ are zero. Moreover, the overall time complexity for lines 4–11 is $\mathcal{O}(\text{size of } S)$ Hence the time complexity of Algorithm 2 is $\mathcal{O}(N_\xi) = \mathcal{O}(\omega^{(\alpha-\beta)d})$.

3.3. Determining directions of basis in the ray-based IPDG method. Previous discussion suggests we consider subsets of Ξ in order to reduce the time complexity. For a single-scale solution $\widetilde{u}$, i.e., $\widetilde{u}$ consisting of wave components with approximately the same frequency, we can restrict $\boldsymbol{\xi} \in \Xi$ to those satisfying (3.2), since only these $\boldsymbol{\xi}$ are close to the true directions. In other words, we may only

---

Algorithm 2 Determine directions of a signal at an observation point $\mathbf{x} = \mathbf{k}/L$.

Input: Ξ: the set of block center $\xi_{\mathbf{i}}$ in GWT; $z_{\mathbf{i},\mathbf{k}}$: the coefficients in GWT for $\xi_{\mathbf{i}} \in \Xi$; η: the relative threshold; ε: the minimum distance between two approximate directions; N_d: the maximum number of directions at each cell center.

Output: $\Theta_{\mathbf{k},\eta}$: the set of directions at $\mathbf{x} = \mathbf{k}/L$.

1: $E \leftarrow \sum_{\mathbf{i}} |z_{\mathbf{i},\mathbf{k}}|^2$
2: $\Theta_{\mathbf{k},\eta} \leftarrow \emptyset, \, e \leftarrow 0$
3: **while** $e \leq E(1 - \eta)$ and $|\Theta_{\mathbf{k},\eta}| < N_d$ **do**
4:     $\mathbf{i}^* \leftarrow \arg\max_{\mathbf{i}} |z_{\mathbf{i},\mathbf{k}}|$,
5:     **if** $z_{\mathbf{i}^*,\mathbf{k}} = 0$ **then**
6:         break this loop
7:     **end if**
8:     $S \leftarrow \{\boldsymbol{\xi} \in \Xi : \left| \boldsymbol{\xi}/|\boldsymbol{\xi}| - \boldsymbol{\xi}_{\mathbf{i}^*}/|\boldsymbol{\xi}_{\mathbf{i}^*}| \right| < \varepsilon\}$
9:     $e \leftarrow e + \sum_{\boldsymbol{\xi}_{\mathbf{i}} \in S} |z_{\mathbf{i},\mathbf{k}}|^2$
10:     for each $\boldsymbol{\xi}_{\mathbf{i}} \in S$, $z_{\mathbf{i},\mathbf{k}} \leftarrow 0$
11:     $\Theta_{\mathbf{k},\eta} \leftarrow \Theta_{\mathbf{k},\eta} \cup \{\boldsymbol{\xi}_{\mathbf{i}^*}/|\boldsymbol{\xi}_{\mathbf{i}^*}|\}$
12: **end while**

---

consider $\boldsymbol{\xi} \in \Xi$ such that

$$e^{2\pi i \boldsymbol{\xi} \cdot \mathbf{x}} \approx e^{i\widetilde{\omega}\nabla\phi_n(\mathbf{x}_0)\cdot\mathbf{x}}$$

or, equivalently,

$$2\pi |\boldsymbol{\xi}| \approx \widetilde{\omega} |\nabla\phi_n(\mathbf{x}_0)| = \widetilde{\omega} \, c(\mathbf{x}_0)^{-1}.$$

Hence, we consider the following annulus:

$$\Xi_{\widetilde{\omega},c} := \left\{ \boldsymbol{\xi} \in \Xi : \frac{\widetilde{\omega}}{2\pi c^*} - W \leq |\boldsymbol{\xi}| \leq \frac{\widetilde{\omega}}{2\pi c_*} + W \right\},$$

where c^* and c_* are the maximum and minimum wave speed in Ω. The size of $\Xi_{\widetilde{\omega},c}$ is $\mathcal{O}(\omega^{(\alpha-\beta)(d-1)})$ when c is constant and $\mathcal{O}(\omega^{(\alpha-\beta)d})$ when c is nonconstant, since the number of $\boldsymbol{\xi} \in \Xi_{\widetilde{\omega},c}$ in the radial direction is $\mathcal{O}(1)$ when c is constant and $\mathcal{O}(\omega^{(\alpha-\beta)})$ when c is nonconstant. We also consider a subset of $\Xi_{\widetilde{\omega},c}$:

$$\Xi_{\widetilde{\omega},c,\mathbf{k}} := \left\{ \boldsymbol{\xi} \in \Xi : \frac{\widetilde{\omega}}{2\pi c(\mathbf{x_k})} - W \leq |\boldsymbol{\xi}| \leq \frac{\widetilde{\omega}}{2\pi c(\mathbf{x_k})} + W \right\},$$

and the size of $\Xi_{\widetilde{\omega},c,\mathbf{k}}$ is $\mathcal{O}(\omega^{(\alpha-\beta)(d-1)})$.

Due to the Shannon sampling theorem, in order to solve for u using finite element methods, the number of degrees of freedom should be at least $\mathcal{O}(\omega)$ in each dimension. Therefore, the total number of observation points at which we extract the directions from $\widetilde{u}$ should be at least $\mathcal{O}(\omega^d)$. Recall that in Algorithm 1 the number of observation points is $L^d \sim \mathcal{O}(\omega^{\beta d})$, $L = 2W$, which is asymptotically less than $\mathcal{O}(\omega^d)$. Instead of increasing the size of W (which would reduce the accuracy), we repeatedly apply Algorithm 2 to subsets of Ξ with shifts on $\widetilde{u}$.

Without loss of generality, we assume that L divides M, where M is the number of tiles in each dimension in the mesh. Recall that by applying Algorithm 2 to the coefficients obtained in Algorithm 1, we can extract the directions at the observation points $\mathbf{x} = \mathbf{k}/L$ for $\mathbf{k} \in \mathbb{Z}_L^d$. In order to extract the directions at the center of
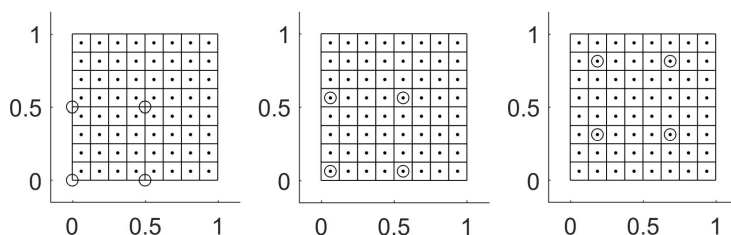
FIG. 2. *An example of applying GWT with shift to $\widetilde{u}$ to extract the directions. Let the number of tiles per dimension $M = 8$ and block size $W = 1$. The dots denote the center of tiles, and the circles denote the observation points of $\widetilde{u}(\mathbf{x})$ after applying Algorithm 1 to $\widetilde{u}(\mathbf{x})$ in the left figure, $\widetilde{u}(\mathbf{x} + h/2)$ in the middle figure, and $\widetilde{u}(\mathbf{x} + (\mathbf{r} + 0.5)h)$ with $\mathbf{r} = (1, 2)$ in the right figure.*

the tiles, we should shift $\widetilde{u}$ by $(\mathbf{r} + 0.5)h$ for $\mathbf{r} \in \mathbb{Z}_{M/L}^d$ and the total number of shifts is $\mathcal{O}(\omega^{(1-\beta)d})$. We demonstrate the idea of shifting in Figure 2. Since the time complexity of applying Algorithm 1 to $\widetilde{u}$ is $\mathcal{O}(\omega^{\alpha d} \log \omega)$, the time complexity for directly applying Algorithm 1 repeatedly with shifts will be $\mathcal{O}(\omega^{(\alpha-\beta)d} \log \omega)$ per observation point, which is too costly.

Instead, we apply the shift theorem of the discrete Fourier transform to reduce the time complexity by repeatedly applying GWT. Suppose $F(\mathbf{n}) = f(\mathbf{n}/N)$ for $n \in \mathbb{Z}_N^d$. Let $\mathbf{s} \in \mathbb{R}^d$ such that $\mathbf{s}N \in \mathbb{Z}^d$. Applying the shift theorem of the discrete Fourier transform,

$$\mathcal{F}_N\big[F(\mathbf{n} + \mathbf{s}N)\big] = e^{i\omega 2\pi \boldsymbol{\xi} \cdot \mathbf{s}} \times \mathcal{F}_N[F(\mathbf{n})],$$

where $\mathcal{F}_N$ is the discrete forward Fourier transform of N samples, and the multiplication on the right-hand side is pointwise. In this way, we can obtain the coefficients of shifted $\widetilde{u}$ by applying the discrete Fourier transform only once. For each shift $\mathbf{r}$, we only apply the pointwise multiplication to a subset of $\Xi_{\widetilde{\omega},c}$ to obtain the coefficients $z_{\mathbf{i},\mathbf{k}}$:

$$\Xi_{\widetilde{\omega},\mathbf{r}} := \cup_{\mathbf{k}} \Xi_{\widetilde{\omega},c,\mathbf{k}}.$$

Then we apply Algorithm 2 to $\Xi_{\widetilde{\omega},\mathbf{r}}$ to determine the directions at the observation points corresponding to the shift. The procedure is shown in Algorithm 3.

Now we discuss the time complexity of Algorithm 3. Let $N_\xi := |\Xi_{\widetilde{\omega},\mathbf{r}}|$. The time complexity for lines 1 and 2 are $\mathcal{O}(\omega^{\alpha d} \log \omega)$ and $\mathcal{O}(\omega^{\beta d} N_\xi)$, respectively. Since the total number of observation points is $\mathcal{O}(\omega^d)$, the time complexity of these two lines is $\mathcal{O}(\omega^{(\alpha-1)d} \log \omega)$ per observation point, which is negligible. The number of iterations of the loop lines 3–12 is $(M/L)^d$, which is $\mathcal{O}(\omega^{-\beta d})$ per observation point. The number of iterations of the loop on lines 5–9 is N_ξ. The time complexity of lines 6–8 is $\mathcal{O}(\omega^{\beta d} \log \omega)$, while the time complexity of line 10 is $\mathcal{O}(N_\xi \omega^{\beta d})$. Therefore, the overall time complexity of Algorithm 3 is $\mathcal{O}(N_\xi \log \omega)$ per observation point. By definition of the set $\Xi_{\widetilde{\omega},\mathbf{r}}$,

(3.4)
$$N_\xi = \begin{cases} \mathcal{O}(\omega^{(\alpha-\beta)(d-1)}) & \text{when the medium is homogeneous,} \\ \mathcal{O}(\omega^{\min\{(\alpha-\beta)(d-1)+\beta d,(\alpha-\beta)d\}}) & \text{otherwise.} \end{cases}$$

We conclude that the overall time complexity of Algorithm 3 is given by (1.1) with an accuracy of $\mathcal{O}(\omega^{\beta-\alpha})$.

Algorithm 3 Determine directions of $\widetilde{u}$ at centers of all tiles.

Input: $\widetilde{u}$: a wavefield; c: the wave speed in Ω; N: the number of spatial samples of $\widetilde{u}$ in each dimension; M: the number of tiles of the mesh in each dimension; W: the block size; $\widetilde{\omega}$: the frequency of $\widetilde{u}$; η: the relative threshold; ε: the minimum distance between two approximate directions; N_d: the maximum number of directions at each cell center.

Output: Θ_K: the directions at the center of each tile.

1: $\hat{u} \leftarrow d$-dimensional forward FFT of $\widetilde{u}$.
2: Compute $h_{\mathbf{i}}(\boldsymbol{\xi})$ for $\boldsymbol{\xi}_{\mathbf{i}} \in \Xi_{\widetilde{\omega},c}$.
3: **for** each shift $\mathbf{r} \in \mathbb{Z}_{M/L}^d$ **do**
4:      $\mathbf{s} \leftarrow \frac{\mathbf{r}+0.5}{M}$.
5:      **for** each $\boldsymbol{\xi}_{\mathbf{i}} \in \Xi_{\widetilde{\omega},\mathbf{r}}$ **do**
6:          $w_{\mathbf{i}}(\boldsymbol{\xi}) \leftarrow h_{\mathbf{i}}(\boldsymbol{\xi})\hat{u}(\boldsymbol{\xi})e^{i\omega 2\pi \boldsymbol{\xi} \cdot \mathbf{s}}$ on $\widetilde{B}_{\mathbf{i}}$.
7:          $t(\boldsymbol{\eta}) \leftarrow w_{\mathbf{i}}(\boldsymbol{\xi}), \boldsymbol{\eta} \equiv \boldsymbol{\xi} \mod L$.
8:          $z_{\mathbf{i},\mathbf{k}} \leftarrow d$-dimensional inverse FFT of $t(\boldsymbol{\eta})$ of size L.
9:      **end for**
10:     Compute $\Theta_{\mathbf{k},\eta}$ using Algorithm 2 applied to $z_{\mathbf{i},\mathbf{k}}$ for $\boldsymbol{\xi}_{\mathbf{i}} \in \Xi_{\widetilde{\omega},\mathbf{r}}$.
11:     $\Theta_{K_{\mathbf{j}}} \leftarrow \Theta_{\mathbf{k},\eta}, \mathbf{j} = (M/L)(\mathbf{k}-1) + \mathbf{r}$.
12: **end for**

3.4. Systematic error in the NMLA. Recall that in our algorithm we apply the fast GWT to represent $f(\mathbf{x}) \in L^2(\mathbb{R}^d)$ by a linear combination of $\phi_{\mathbf{i},\mathbf{k}}$ by assuming that $\phi_{\mathbf{i},\mathbf{k}}$ differs from a Gaussian wave packet by a negligible error. However, we will show that this small error is $\mathcal{O}(1)$ relative to the L^2-norm of f. This could deteriorate the convergence rate as the frequency ω gets large.

Let $\chi(\mathbf{x})$ be the characteristic function of $[-1,1]^d$. The Gaussian wave packets in the frequency domain are given by

$$\widehat{\phi}_{\mathbf{i},\mathbf{k}}(\boldsymbol{\xi}) := \frac{1}{L^{d/2}} e^{-|\boldsymbol{\xi}-\boldsymbol{\xi}_{\mathbf{i}}|^2/\sigma^2} \chi\left(\frac{\boldsymbol{\xi}-\boldsymbol{\xi}_{\mathbf{i}}}{2\sigma}\right).$$

Define the exact Gaussian wave packets $\phi^*_{\mathbf{i},\mathbf{k}}(\mathbf{x})$ in the frequency domain by

$$\widehat{\phi^*}_{\mathbf{i},\mathbf{k}}(\boldsymbol{\xi}) := \frac{1}{L^{d/2}} e^{-|\boldsymbol{\xi}-\boldsymbol{\xi}_{\mathbf{i}}|^2/\sigma^2},$$

where $\phi_{\mathbf{i},\mathbf{k}}(\mathbf{x}) \approx \phi^*_{\mathbf{i},\mathbf{k}}(\mathbf{x})$. Indeed, we can estimate the L^2 error in each of the Gaussian wave packet approximations by

$$\begin{aligned}
\left\|\phi_{\mathbf{i},\mathbf{k}}(\mathbf{x}) - \phi^*_{\mathbf{i},\mathbf{k}}(\mathbf{x})\right\|^2_{L^2(\mathbb{R}^d)} &= \frac{1}{L^d} \int_{\mathbb{R}^d} e^{-2|\boldsymbol{\xi}-\boldsymbol{\xi}_{\mathbf{i}}|^2/\sigma^2} \left(1 - \chi\left(\frac{\boldsymbol{\xi}-\boldsymbol{\xi}_{\mathbf{i}}}{2\sigma}\right)\right)^2 d\boldsymbol{\xi} \\
&= \frac{1}{4^d} \int_{\mathbb{R}^d} e^{-2|\boldsymbol{\xi}|^2} \left(1 - \chi\left(\boldsymbol{\xi}/2\right)\right)^2 d\boldsymbol{\xi} \\
&< \frac{1}{4^d} \int_{|\boldsymbol{\xi}|>2} e^{-2|\boldsymbol{\xi}|^2} d\boldsymbol{\xi} \approx (9.924 \times 10^{-6})^d.
\end{aligned}$$

Define an operator $\mathcal{S}$ on $L^2(\mathbb{R}^d)$ given by

$$\mathcal{S}(f) : f(\mathbf{x}) = \sum_{\mathbf{i},\mathbf{k}} z_{\mathbf{i},\mathbf{k}} \phi_{\mathbf{i},\mathbf{k}}(\mathbf{x}) \mapsto \sum_{\mathbf{i},\mathbf{k}} z_{\mathbf{i},\mathbf{k}} \phi^*_{\mathbf{i},\mathbf{k}}(\mathbf{x}).$$

We have the following lemma whose proof is given in Appendix A.

LEMMA 3.1. *For $d = 1, 2, 3$, there is a constant $\varepsilon \sim \mathcal{O}(1)$ such that*

$$\|f - \mathcal{S}(f)\|_{L^2(\mathbb{R}^d)} \leq \varepsilon \|f\|_{L^2(\mathbb{R}^d)}.$$

Although it is not clear from the proof of Lemma 3.1 that $\varepsilon < 1$, numerical studies suggest that this is the case. In the following discussion, we assume that $\varepsilon < 1$ holds. For any integer n, we can write

$$(3.5) \qquad f = \sum_{r=0}^{n-1} \mathcal{S}(I - \mathcal{S})^r f + (I - \mathcal{S})^n f.$$

Using the lemma, we have $\|(I - \mathcal{S})^n f\|_{L^2(\mathbb{R}^d)} \lesssim \varepsilon^n \|f\|_{L^2(\mathbb{R}^d)} \to 0$ as $n \to \infty$. Moreover,

$$f(\mathbf{x}) = \sum_{r=0}^{\infty} \mathcal{S}(I - \mathcal{S})^r f(\mathbf{x}) = \sum_{\mathbf{i},\mathbf{k}} \left(z_{\mathbf{i},\mathbf{k}} + \sum_{r=1}^{\infty} e_{\mathbf{i},\mathbf{k}}^r \right) \phi_{\mathbf{i},\mathbf{k}}^*(\mathbf{x}),$$

where $e_{\mathbf{i},\mathbf{k}}^r$ are the coefficients in the fast GWT of $(I - \mathcal{S})^r f(\mathbf{x})$. Define $e_{\mathbf{i},\mathbf{k}} := \sum_{r=1}^{\infty} e_{\mathbf{i},\mathbf{k}}^r$. We see that our interpretation of $z_{\mathbf{i},\mathbf{k}}$ in the NMLA differs from an exact Gaussian wave packet representation of f in (3.5) by $e_{\mathbf{i},\mathbf{k}}$. Recall that in our NMLA, we choose the directions by considering $z_{\mathbf{i},\mathbf{k}}$ with relatively large magnitude. Therefore the difference in the magnitude of $z_{\mathbf{i},\mathbf{k}}$ and $z_{\mathbf{i},\mathbf{k}} + e_{\mathbf{i},\mathbf{k}}$ contributes to a systematic error. To estimate the size of $e_{\mathbf{i},\mathbf{k}}$, one can show that [3, Lemma 3.1] whenever $f(\mathbf{x}) = \sum_{\mathbf{i},\mathbf{k}} z_{\mathbf{i},\mathbf{k}} \phi_{\mathbf{i},\mathbf{k}}(\mathbf{x})$ there are positive constants $C_1, C_2 \sim \mathcal{O}(1)$ such that

$$C_1 \|f\|_2 \leq \left(\sum_{\mathbf{i},\mathbf{k}} |z_{\mathbf{i},\mathbf{k}}|^2 \right)^{\frac{1}{2}} \leq C_2 \|f\|_2.$$

Note that $\sum_{r=1}^{\infty} (I - S)^r f(\mathbf{x}) = \sum_{\mathbf{i},\mathbf{k}} e_{\mathbf{i},\mathbf{k}} \phi_{\mathbf{i},\mathbf{k}}(\mathbf{x})$. Hence there is a constant $C \sim \mathcal{O}(1)$ such that

$$\left(\sum_{\mathbf{i},\mathbf{k}} |e_{\mathbf{i},\mathbf{k}}|^2 \right)^{\frac{1}{2}} \leq C \left\| \sum_{r=1}^{\infty} (I - \mathcal{S})^r f \right\|_2 \leq \frac{C\varepsilon}{1 - \varepsilon} \|f\|_2,$$

which shows that the size of the systematic error is at most $\mathcal{O}(1)$ relative to the L^2-norm of the signal f.

4. Numerical examples. In this section, we perform various experiments to investigate the performance of the NMLA (Algorithm 3) and the ray-based IPDG method in dimension $d = 2$. In all the experiments, we will use the following frequencies for different choices of k:

$$\omega = 2^k \times 10\pi, \quad \widetilde{\omega} = \sqrt{2^k} \times 10\pi.$$

Under this setting, $\widetilde{\omega} \sim \mathcal{O}(\omega^{0.5})$ or, equivalently, $\alpha = 0.5$. We will consider the wavefields u_1–u_7 listed in Table 2. Unless otherwise stated, we will assume the computational domain to be $\Omega = [0, 1]^2$. For $\omega = 20\pi$, these wavefields are shown in Figure 3. For each k, we denote the wavefields with reduced frequency $\widetilde{\omega}$ corresponding to u_i by $\widetilde{u}_i$ ($i = 1, 2, \ldots, 7$), respectively.

TABLE 2
Problem sets.

Problem set	Wave speed	Wave field	Source f
1		$u_1 = e^{i\omega x_1}$	
2		$u_2 = e^{i\omega x_1} + e^{i\omega x_2}$	
3	1	$u_3 = \sqrt{\omega} H_0^{(1)}(\omega \lvert \mathbf{x} - \mathbf{x}_1 \rvert)$	0
4		$u_4 = \sqrt{\omega} H_0^{(1)}(\omega \lvert \mathbf{x} - \mathbf{x}_1 \rvert)$ $+ 0.5\sqrt{\omega} H_0^{(1)}(\omega \lvert \mathbf{x} - \mathbf{x}_2 \rvert)$	
5		$u_5 = $ free space solution	$f_5 := 10^4 e^{-10^4 \lvert \mathbf{x} - \mathbf{x}_3 \rvert^2}$
6	$c_6(\mathbf{x})$	$u_6 = $ free space solution	$f_6 := 10^4 e^{-10^4 \lvert \mathbf{x} - \mathbf{x}_4 \rvert^2}$
7	$c_7(\mathbf{x})$	$u_7 = $ free space solution	$f_7 := 10^4 e^{-10^4 \lvert \mathbf{x} - \mathbf{x}_4 \rvert^2}$

$c_6(\mathbf{x}) := 1 - 0.5 e^{-100[(y-0.4)^2 + (x+0.5y-0.7)^2)]}$, $c_7(\mathbf{x}) := $ a scaled smooth Marmousi model,
$\mathbf{x} := (x_1, x_2), \mathbf{x}_1 := (2, 2), \mathbf{x}_2 := (-1, 2), \mathbf{x}_3 := (0.5, 0.5), \mathbf{x}_4 := (0.5, 0.1)$.
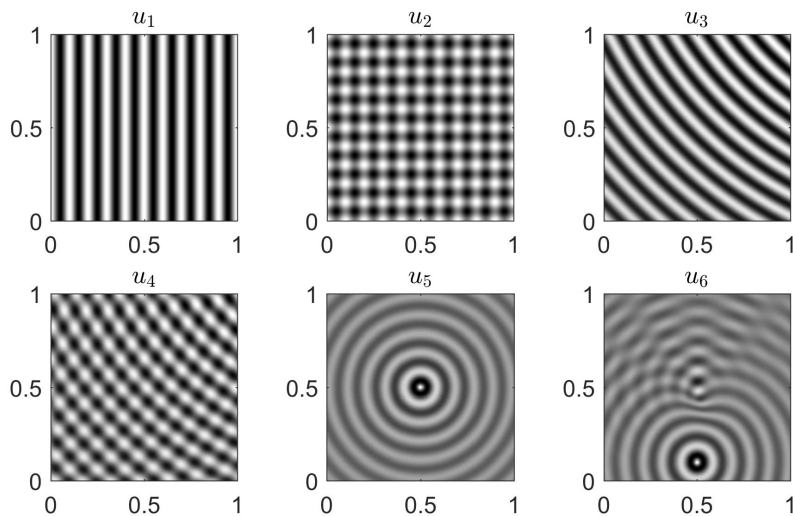
FIG. 3. *The real part of u_1–u_6 with $\omega = 20\pi$ in the computational domain Ω.*

4.1. The accuracy of the NMLA. In this section, we test the accuracy of the NMLA by applying NMLA to the exact solution $\widetilde{u}_i$ ($i = 1, 2, 3, 4$) on Ω.

Since $\widetilde{u}_1$ and $\widetilde{u}_2$ are periodic in Ω, we can directly apply our NMLA to uniform samples of $\widetilde{u}_1$ and $\widetilde{u}_2$ in Ω. However, $\widetilde{u}_3$ and $\widetilde{u}_4$ are nonperiodic in Ω. Instead, for $\widetilde{u}_3$, we consider $\widetilde{u}_3 (2\mathbf{x} - 0.5)$ multiplied by the following window function for $\mathbf{x} \in \Omega$:

$$w(\mathbf{x}) = w_0(x_1) w_0(x_2), \quad w_0(x) = \begin{cases} (1 + e^{-\frac{\lambda\mu}{2}}) / (1 + e^{-\lambda(x - \mu/2)}) & \text{if } x < \mu, \\ w_0(1-x) & \text{if } x > 1 - \mu, \\ 1 & \text{otherwise} \end{cases}$$

with $\lambda = 50$, and $\mu = 0.125$. The window functions are illustrated in Figure 4. Afterwards, we apply NMLA to the samples of $\widetilde{u}_3 (2\mathbf{x} - 0.5) w(\mathbf{x})$ for $\mathbf{x} \in \Omega$. Since the size of the range of $2\mathbf{x} - 0.5$ is twice the size of Ω in each dimension, when we apply
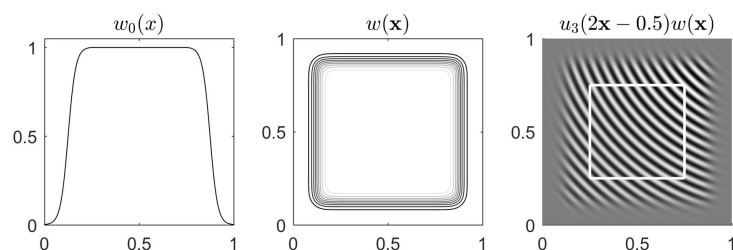
FIG. 4. *Left: Plot of the function $w_0(x)$. Middle: The contour plot of window function $w(\mathbf{x})$. Right: The exact solution u_3 with frequency $\omega = 20\pi$ rescaled and multiplied by $w(\mathbf{x})$. The square shows u_3 on Ω after rescaling.*

NMLA to $\widetilde{u}_3\,(2\mathbf{x} - 0.5)\,w(\mathbf{x})$, the number of samples N, the number of tiles M, and the block size W are twice those used when applying NMLA to $\widetilde{u}_3(\mathbf{x})$ on Ω. Then the directions are obtained from the corresponding observation points in Ω. We do the same for $\widetilde{u}_4$.

For the solutions u_1 and u_3, we apply the NMLA with parameters

$$(N, M, N_d) = \Big(\left\lceil \frac{\widetilde{\omega}}{2\pi W} \right\rceil \times 4W,\ W,\ 1 \Big).$$

Here η and ε are irrelevant as $N_d = 1$. For the solutions u_2 and u_4, there are two true directions at each observation point. For these solutions, we apply the NMLA with parameters (relative to Ω)

$$(N, M, \eta, \varepsilon, N_d) = \Big(\left\lceil \frac{\widetilde{\omega}}{2\pi W} \right\rceil \times 4W,\ W,\ 0,\ 0.75,\ 2 \Big).$$

Since the minimum distance between the two directions at each tile center $\mathbf{x}_K$ is approximately 1.57 and 1.2, respectively, by choosing $\varepsilon = 0.75$, we keep all true directions in Algorithm 2.

Let $\widehat{\Theta}_K$ be the set of approximate directions from NMLA, and Θ_K be the correct direction at the center of K. We define the direction error on K by

$$(4.1) \qquad\qquad e(K) := \sup_{\mathbf{d} \in \Theta_K} \inf_{\widehat{\mathbf{d}} \in \widehat{\Theta}_K} \left| \mathbf{d} - \widehat{\mathbf{d}} \right|.$$

Then we take the direction error of NMLA to be the average of $e(K)$ over all tiles K. For $k = 1, 2, \ldots, 18$, we plot the direction errors of NMLA applying to u_i ($i = 1, 2, 3, 4$) with $W \sim \mathcal{O}(1)$ ($\beta = 0$) in Figure 5 and $W = \left\lceil R\omega^{0.25} \right\rceil$ ($\beta = 0.25$) in Figure 6.

These results show that for u_1 and u_2, which consist of plane waves, our NMLA achieves the optimal convergence rate for the directions as $\omega \to \infty$ in all the test cases. For u_3 and u_4, the convergence rate is optimal when $W = \left\lceil R\omega^{0.25} \right\rceil$, but halved when $W = \mathcal{O}(1)$ and $\omega/2\pi \gtrsim 10^4$ or $\widetilde{\omega}/2\pi \gtrsim 220$. We can also observe that for these cases, the convergence rate is better for larger W.

We have shown in section 3.4 that there is an $\mathcal{O}(1)$ systematic error in the coefficient $z_{\mathbf{i},\mathbf{k}}$ in the NMLA. To see how this error affects the accuracy, we apply the NMLA to the "one-term-correction" of $\widetilde{u}$ given by $\mathcal{S}\widetilde{u} + \mathcal{S}(I - \mathcal{S})\widetilde{u}$ for $W = 2$ and 4, $k = 1$ to 15. The numerical errors in the directions are exactly the same as the result for $\widetilde{u}$ with only a few exceptions, and the differences in the error for those exceptions are negligible. This result suggests that the systematic error does not account for the deterioration in the accuracy of the above examples.
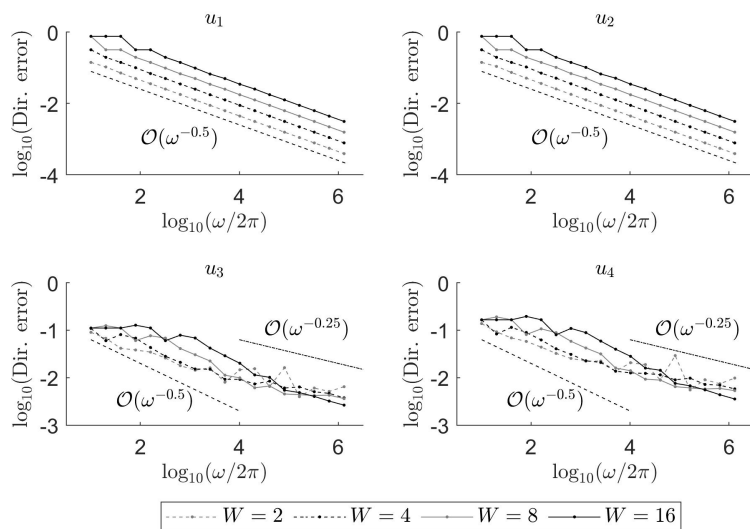
FIG. 5. *The direction errors of NMLA applying to u_i $(i = 1, 2, 3, 4)$ with $W \sim \mathcal{O}(1)$.*
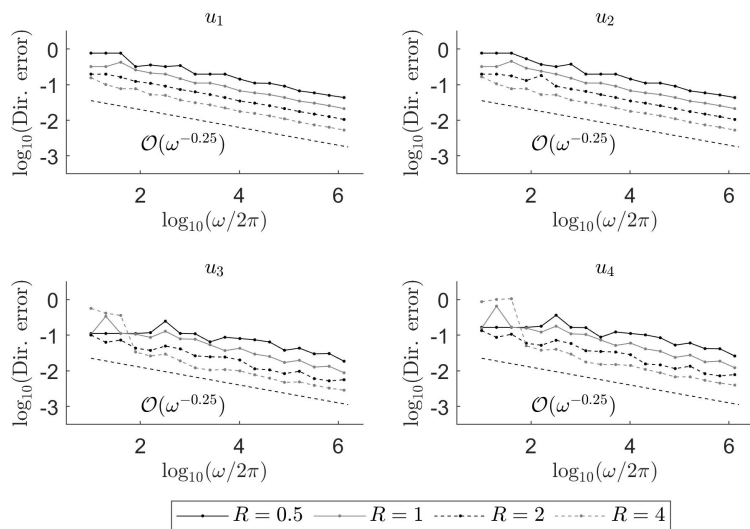
FIG. 6. *The direction errors of NMLA applying to u_i $(i = 1, 2, 3, 4)$ with $W = \lceil R\omega^{0.25} \rceil$.*

Recall that L is the size of the extended blocks (cf. Figure 1) and also the number of observation points in the spatial domain per dimension per shift. We note that we have set $\sigma = W/2$ and $L = 2W$. Therefore, the parameters L and σ are $\mathcal{O}(1)$ in Figure 5 and $\mathcal{O}(\omega^{0.25})$ in Figure 6, respectively.

As a remedy, we consider increasing L for the example u_3 and $W = 4$. Now, we choose L to be larger than $2W = 8$, $\sigma = L/4$. We compute and show the direction errors with different constants L, and $L = 4 \left\lceil \sqrt{\widetilde{\omega}/10\pi} \right\rceil \sim \mathcal{O}(\omega^{0.25})$ in Figure 7. It shows that the accuracy of our NMLA when $L \sim \mathcal{O}(\omega^{0.25})$ is optimal. It suggests that for solutions with curved wavefronts, the parameter L should increase
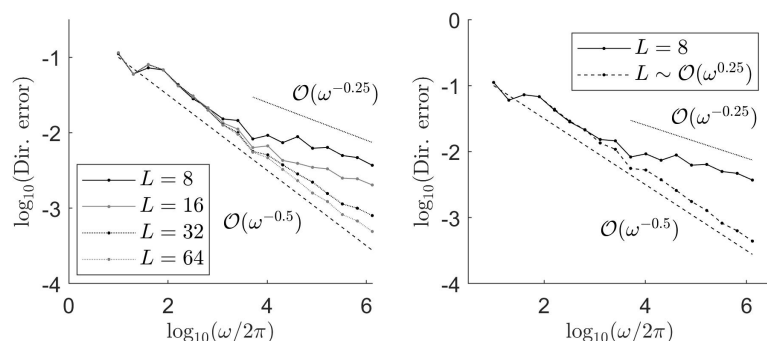
FIG. 7. *The direction errors of our NMLA applying to $\widetilde{u}_3$ with $W = 4$ and different choices of L.*

with the frequency in order to achieve optimal accuracy. Following the discussion in section 3.3, when we choose $L \sim \mathcal{O}(\omega^{0.25})$, the time complexity of our NMLA for a homogeneous medium is unchanged, while the time complexity for an inhomogeneous medium becomes $\mathcal{O}(\omega^{\min\{(\alpha-\beta)(d-1)+0.25d,(\alpha-\beta)d\}})$. However, here we will not further investigate how to choose the parameter L to obtain the optimal accuracy when applying NMLA to a general solution.

In the following numerical examples, we will use the original settings and only consider $\omega/2\pi \leq 160$. We do not observe any deterioration of accuracy in this range of frequency.

4.2. NMLA and the GWT. In Figure 8, we display the magnitude of coefficients (in $\log_{10}$ scale) in the GWT of u_2 and u_4 with block size $W = 4$ at the tile $\mathbf{k} = (4, 4)$ using the same set of parameters for NMLA as in section 4.1. We observe that the coefficients with significant magnitude appear near the correct directions and the set $\Xi_{\widetilde{\omega},c}$ captures the significant coefficients.

Next we define the relative magnitude of coefficients of the Gaussian wave packet in the direction at θ:

$$(4.2) \qquad m(\theta) = \left(\frac{\max\limits_{\arg \boldsymbol{\xi_i} = \theta, \boldsymbol{\xi_i} \in \Xi_{\widetilde{\omega},c}} |z_{\mathbf{i},\mathbf{k}}|^2}{\sum_{\boldsymbol{\xi_i} \in \Xi_{\widetilde{\omega},c}} |z_{\mathbf{i},\mathbf{k}}|^2} \right)^{1/2}.$$

Since $\Xi_{\widetilde{\omega},c}$ is a subset of Cartesian points, $m(\theta)$ is a discrete signal. We display $m(\theta)$ of u_2 and u_4 at the tile $\mathbf{k} = (4, 4)$, the exact directions and the approximate directions by NMLA in Figure 9. We observe that, as ω gets larger, the approximate directions by NMLA approach the exact directions. Also, for u_4, in the neighborhood of a correct direction there are a few extra significant coefficients. This shows the redundancy of NMLA for nonplanar waves.

4.3. Convergence for the Helmholtz problems. In this section, we apply NMLA to solve Helmholtz problems. We will consider the solutions u_2 and u_4 in Ω.

Case of u_2: For a reduced frequency $\widetilde{\omega}$, we solve the Helmholtz equations with impedance boundary conditions using the standard IPDG method with bilinear basis. The mesh size is $\widetilde{h} = 1/(4 \lceil \frac{\omega}{\pi} \rceil)$ and the penalty parameter is taken as $\mathbf{a} = 5$.
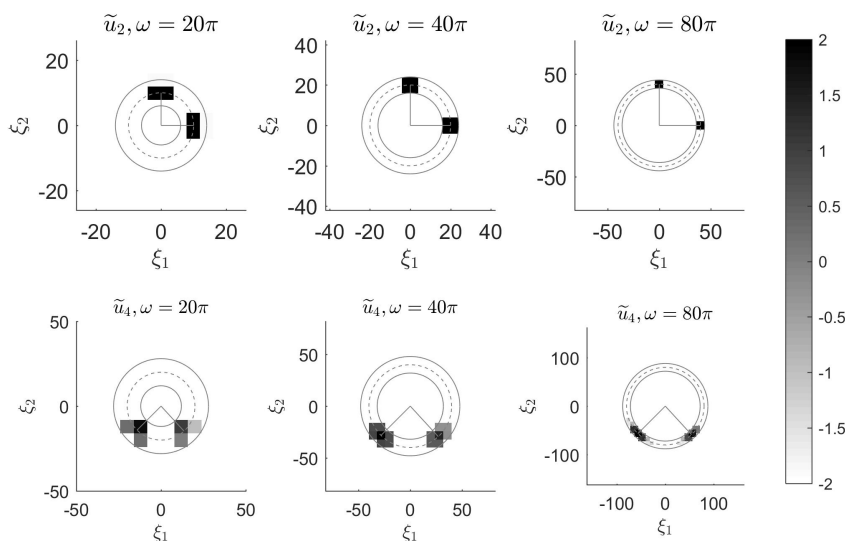
FIG. 8. *The magnitude of coefficient of GWT (in log scale) for u_2 and u_4 with different $\widetilde{\omega}$. The solid white circles represent $\Xi_{\widetilde{\omega},c}$. The dotted white circles represent $\widetilde{\omega}/2\pi$. The gray lines represent the true directions.*
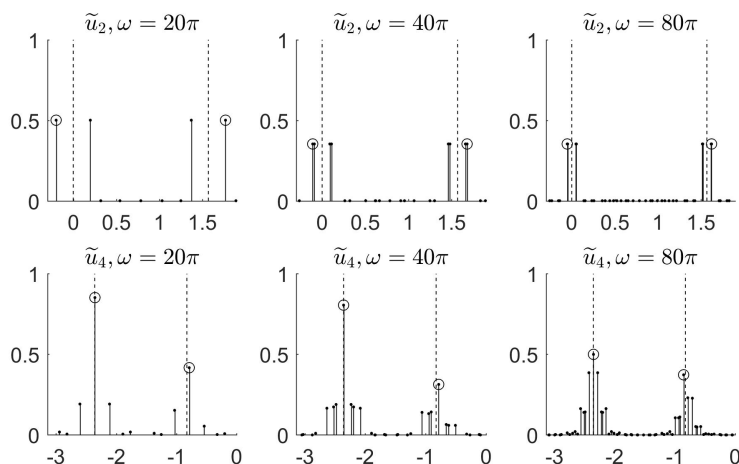

FIG. 9. *The relative magnitude $m(\theta)$ for $\widetilde{u}_2$ and $\widetilde{u}_4$ with different frequency $\widetilde{\omega}$. Each blue stem in the plot of $m(\theta)$ has length $m(\theta)$. The dotted black lines represent the correct direction. The circles represent the approximate directions selected by NMLA.*

Afterwards, we apply the NMLA using the following parameters with $W = 2$:

$$(N, M, N_d) = \left(\left\lceil \frac{\widetilde{\omega}}{2\pi W} \right\rceil \times 4W, \ \left\lceil \frac{\omega}{\pi W} \right\rceil W, \ 1 \right).$$

Case of u_4: We consider $\widetilde{u}_4$ on an extended domain $\Omega' = [-0.5, 1.5]^2$. We solve the Helmholtz equation with impedance boundary conditions for $\widetilde{u}_4$ using the standard
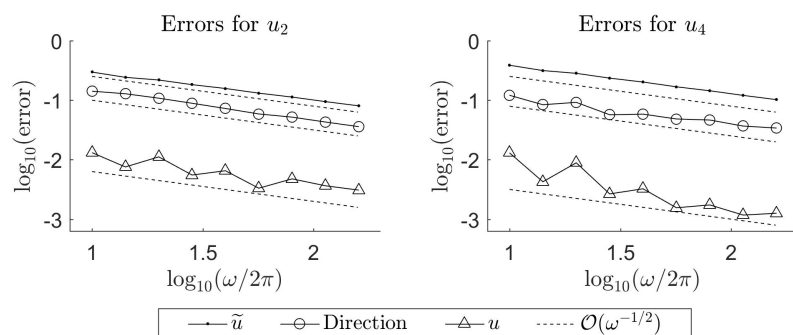
FIG. 10. *The relative L^2 error of $\widetilde{u}$, the direction error, and the relative L^2 error of u.*
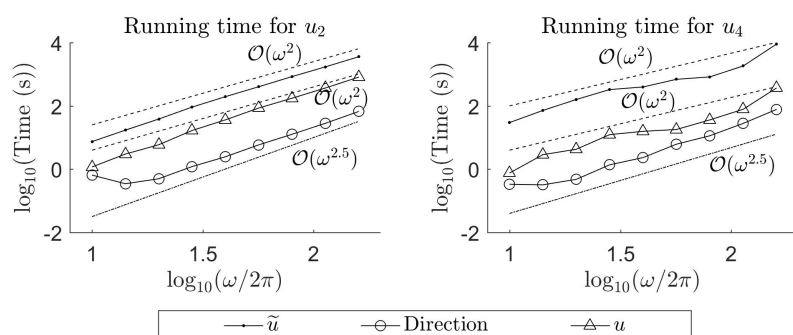
FIG. 11. *The running time of solving $\widetilde{u}$, NMLA, and solving u.*

IPDG method with bilinear basis with penalty parameter $\mathbf{a} = 5$ and mesh size $\widetilde{h} = 1/(4 \left\lceil \frac{\omega}{\pi} \right\rceil)$. Then we multiply the numerical solution of $\widetilde{u}_4(2\mathbf{x} - 0.5)$ by the window function $w(\mathbf{x})$ for $\mathbf{x} \in \Omega$ and apply NMLA using the following parameters (relative to Ω) with $W = 2$:

$$(N, M, N_d) = \left(\left\lceil \frac{\widetilde{\omega}}{2\pi W} \right\rceil \times 4W, \ \left\lceil \frac{\omega}{\pi W} \right\rceil W, \ 0, \ 0.75, \ 2 \right).$$

Finally, we incorporate the approximate directions into the ray-based IPDG method and solve the Helmholtz equations with impedance boundary conditions, using mesh size $h = 1/M$ and $\mathbf{a} = 5$.

The errors for u_2 and u_4 and the running times are shown in Figures 10 and 11, respectively. Figure 10 shows that the direction error and the L^2-error for u_2 and u_4 all decay like $\mathcal{O}(\omega^{-0.5})$. Also, the running time for the NMLA is $\mathcal{O}(\omega^{2.5})$, or $\mathcal{O}(\omega^{0.5})$ per observation point, as predicted.

4.4. NMLA near a point source. In this section, we consider the fifth problem in Table 2. We apply NMLA to $\widetilde{u}_5$ with $\widetilde{\omega} = 80\pi$ on the extended domain Ω', multiplied by the window function $w(\mathbf{x})$ as described in previous sections. We use the following parameters for the NMLA:

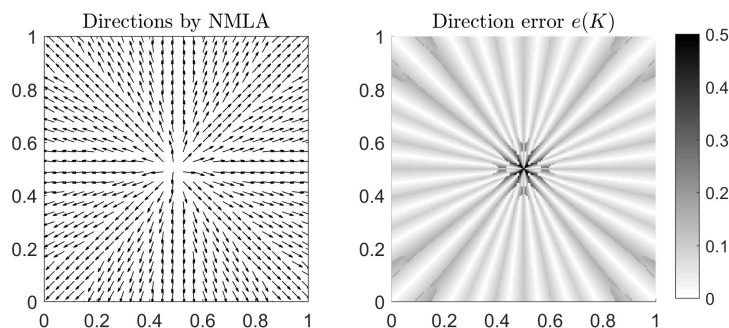$$(N, M, N_d) = \left(\left\lceil \frac{\widetilde{\omega}}{2\pi W} \right\rceil \times 8W, \ 320, \ 1 \right).$$

FIG. 12. *The approximate directions and the direction errors of NMLA applying to $\widetilde{u}_5$, at different locations in the domain Ω.*
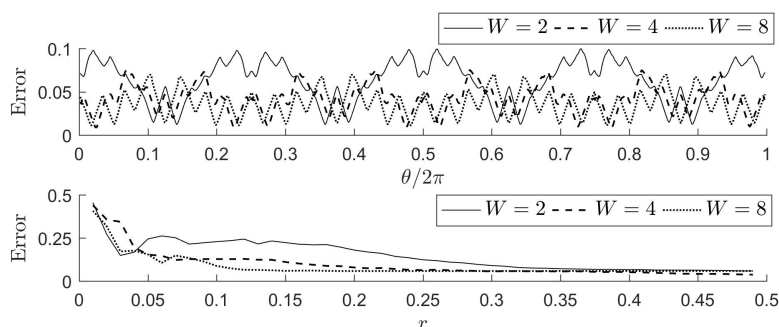

FIG. 13. *The average of $e(r, \theta)$ for fixed θ (upper figure) and fixed r (lower figure).*

For $W = 8$, we plot the directions and the direction errors $e(K)$ for each tile K in Figure 12. Next, we treat the direction error $e(K)$ as a value at the cell center $\mathbf{x}_K$, and change the coordinates from (x_1, x_2) to (r, θ), where r is the distance to the source location and θ is the polar angle. By interpolation, we obtain $e(r, \theta)$. In Figure 13, we show the average of $e(r, \theta)$ for each r and for each θ, respectively. We observe that the direction error increases when approaching the source location. On the other hand, the direction error oscillates as θ increases. We note that in the NMLA, we sample the directions on a circle using a Cartesian grid, which makes the sampling accuracy vary in different directions.

Then, in Figure 14, we show the relative magnitude of coefficients, $m(\theta)$, in the GWT of $\widetilde{u}_5$ for $\widetilde{\omega} = 80\pi$, using the following parameters of NMLA:

$$(N, M, \eta, \varepsilon, N_d) = \left(\left\lceil \frac{\widetilde{\omega}}{2\pi W} \right\rceil \times 8W, \ 32, \ 0.5, \ 0.25, \ 4 \right).$$

It shows that the size of the coefficients in the GWT has smaller variance and the number of approximation directions by NMLA is larger when the location is closer to the source. Also, in this example, the direction error is zero at each of the locations, although there is redundancy of the directions near the source.

4.5. Caustics. In this section, we consider the sixth problem in Table 2, where the solution u_6 has caustics approximately at $\mathbf{x} = (0.5, 0.5)$. We apply NMLA to $\widetilde{u}_6$ with $\widetilde{\omega} = 80\pi$ on the extended domain Ω', multiplied by the window function $w(\mathbf{x})$
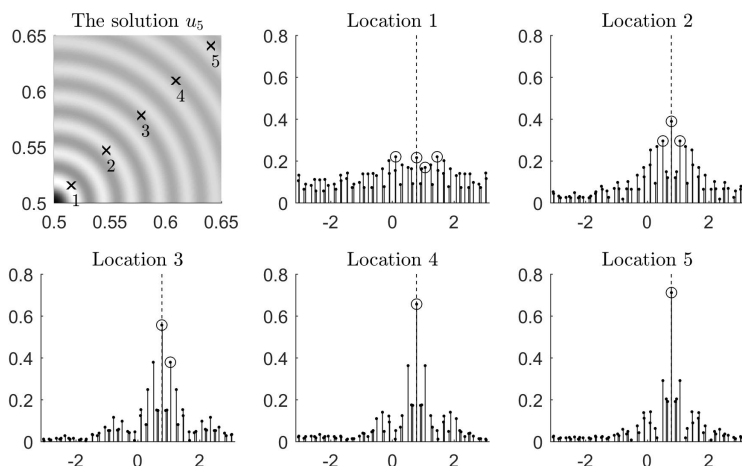
FIG. 14. *The relative magnitude $m(\theta)$ for u_5 at different locations in Ω. The locations are shown in the upper left figure. For other figures, the vertical axis is $m(\theta)$ and the horizontal axis is θ. The red circles indicate the approximate directions by NMLA and the dotted lines are the correct directions.*
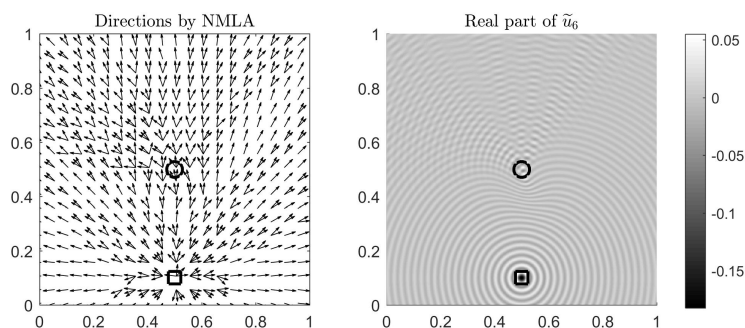

FIG. 15. *The approximate directions by NMLA applied to u_6 and the real part of u_6 on Ω.*

as described in previous sections. The parameters of NMLA are given by

$$(N, M, N_d) = \left(\left\lceil \frac{\widetilde{\omega}}{2\pi W} \right\rceil \times 8W, \ 80, \ 1 \right).$$

We plot the directions in Figures 15 and 16. We can observe that there are more approximate directions near the source and caustics.

Next, in Figure 17, we plot the relative magnitudes of coefficients, $m(\theta)$, in the GWT of $\widetilde{u}_6$ for $\widetilde{\omega} = 80\pi$ at various observation points. We use the following parameters for NMLA:

$$(N, M, \eta, \varepsilon, N_d) = \left(\left\lceil \frac{\widetilde{\omega}}{2\pi W} \right\rceil \times 8W, \ 16, \ 0.25, \ 0.25, \ 4 \right).$$

We see that the approximation directions match our intuition of the directions.

Then, we solve the sixth problem in Table 2 on the computational domain $\Omega'' := [0.25, 0.75]^2$ supplemented with the Cauchy boundary condition on $x_2 = 0.25$ and
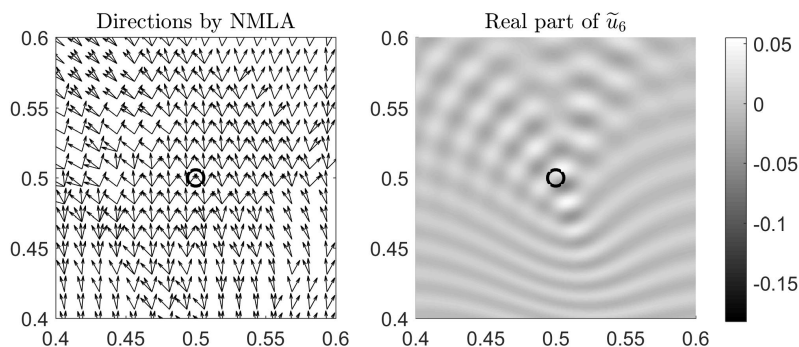
FIG. 16. *The approximate directions by NMLA applied to u_6 and the real part of u_6 on $[0.4, 0.6]^2$.*
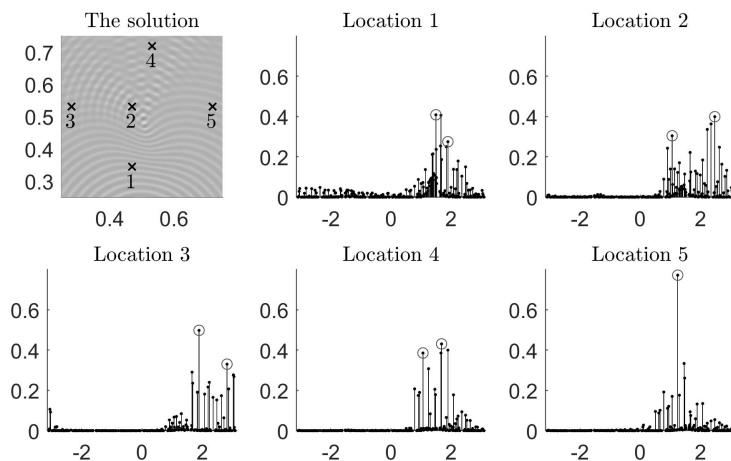

FIG. 17. *The relative magnitude $m(\theta)$ for u_6 at different locations in Ω. The locations are shown in the upper left figure. For other figures, the vertical axis is $m(\theta)$ and the horizontal axis is θ. The red circle indicates the approximate directions by NMLA.*

PML conditions on the other three sides. To solve for u_6, we first apply NMLA to $\widetilde{u}_6$ on Ω to get approximate directions. Then we incorporate these directions into the basis of the IPDG system. The penalty parameter is taken as $\mathbf{a} = 20$ and the parameters for the NMLA (relative to Ω) are given by

$$(N, M, \eta, \varepsilon, N_d) = \left(\left\lceil \frac{\widetilde{\omega}}{2\pi W} \right\rceil \times 8W, \ \left\lceil \frac{\omega}{4\pi W} \right\rceil \times 4W, \ 0, \ 0.25, \ 4 \right).$$

The errors for the solution and the running times for carrying out NMLA and solving the IPDG system are given in Figure 18. It shows that the ray-based IPDG method converges with order $\mathcal{O}(\omega^{-0.5})$ in terms of relative L^2-errors and the computational costs for performing NMLA and solving the IPDG system have a time complexity of $\mathcal{O}(\omega^{2.5})$ and $\mathcal{O}(\omega^3)$, respectively, as expected.

4.6. The Marmousi model. In this section, we consider the seventh problem in Table 2. We rescale the Marmousi model in the domain $[3\text{km}, 7\text{km}] \times [0\text{km}, 2.5\text{km}]$
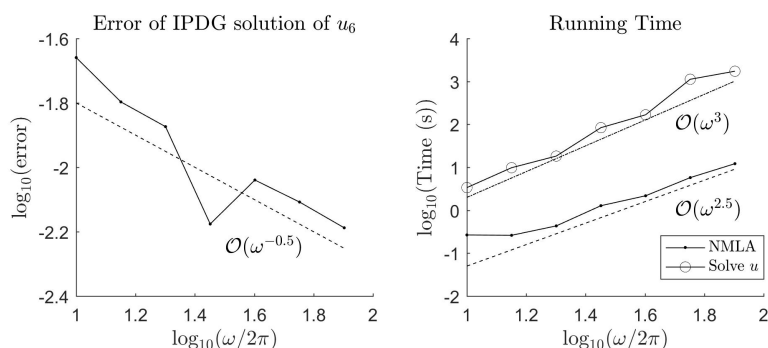
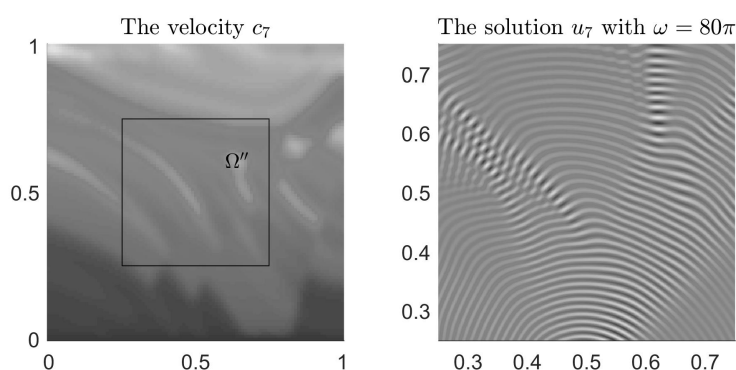FIG. 18. *The errors and the running time in the convergence test for u_6 on Ω''.*

FIG. 19. *The velocity c_7 in Ω and the solution u_7 with $\omega = 80\pi$ in Ω''. The circle indicates the location of the source.*

into $\Omega := [0,1]^2$ and normalize the velocity by a factor of 4500 km/s. The image of the Marmousi model and the real part of the solution are shown in Figure 19. We can see that in the domain $\Omega'' := [.25, .75]^2$, there are several strong directions mixed up with weaker ones.

We plot, in Figure 20, the relative magnitudes of coefficients, $m(\theta)$, in the GWT of $\widetilde{u}_6$ for $\widetilde{\omega} = 80\pi$ at various observation points. We use the following parameters for the NMLA:

$$(N, M, \eta, \varepsilon, N_d) = \left(\left\lceil \frac{\widetilde{\omega}}{2\pi W} \right\rceil \times 8W, 16, \ 0.1, \ 0.25, \ 4 \right).$$

Finally, we solve the seventh problem on the computational domain Ω'' supplemented with the Cauchy boundary condition on $x_2 = 0.25$ and PML conditions on the other three sides. To solve for u_7, we first apply NMLA to $\widetilde{u}_7$ on Ω to get approximate directions. Then we incorporate these directions into the basis of the IPDG system. The penalty parameter is taken as $\mathbf{a} = 20$ and the parameters for the NMLA (relative to Ω) are given by $W = 2$ and

$$(N, M, \eta, \varepsilon, N_d) = \left(\left\lceil \frac{\widetilde{\omega}}{2\pi W} \right\rceil \times 8W, \ \left\lceil \frac{\omega}{4\pi W} \right\rceil \times 4W, \ 0, \ 0.25, \ 4 \right).$$
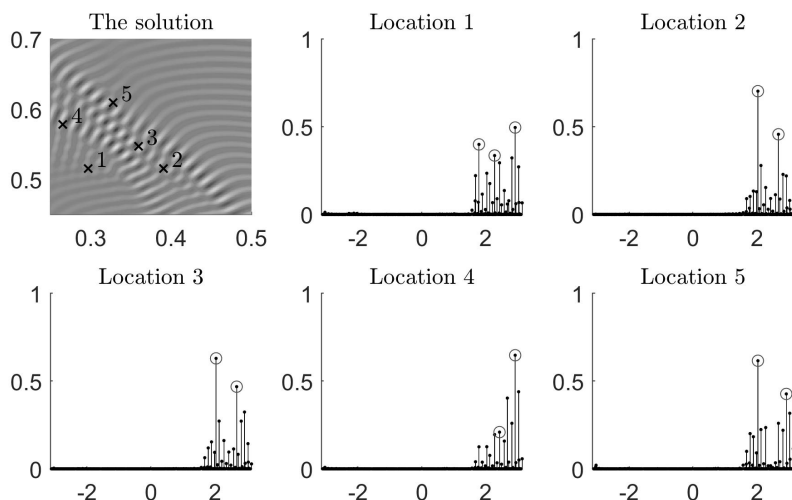
FIG. 20. *The relative magnitude $m(\theta)$ for u_7 at different locations in Ω. The locations are shown in the upper left figure. For other figures, the vertical axis is $m(\theta)$ and the horizontal axis is θ. The red circle indicates the approximate directions by NMLA.*
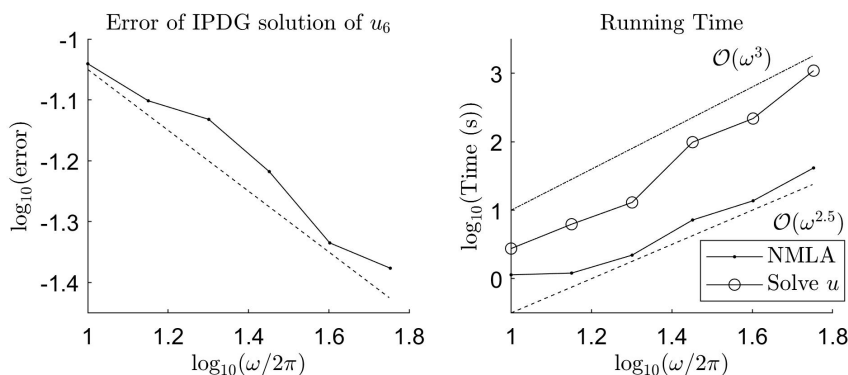

FIG. 21. *The errors and the running time in the convergence test for u_7 on Ω''.*

The errors for the solution and the running times for carrying out NMLA and solving the IPDG system are given in Figure 21. It shows that the ray-based IPDG method converges with order $\mathcal{O}(\omega^{-0.5})$ in terms of relative L^2-errors and the computational costs for performing NMLA and solving the IPDG system have a time complexity of $\mathcal{O}(\omega^{2.5})$ and $\mathcal{O}(\omega^3)$, respectively.

5. Conclusion. We present a novel NMLA method via the GWT, and we further incorporate it into a hybrid method for solving the high-frequency Helmholtz equation in heterogeneous media. Numerical results demonstrate that the NMLA method can achieve an accuracy of $\mathcal{O}(\omega^{-1/2})$ with a time cost of $\mathcal{O}(\omega^{1/2})$ per observation point when applied to an analytic or numerical solution of the Helmholtz equations with frequency $\mathcal{O}(\omega^{1/2})$. Also, apparently almost no pollution effect is observed in the solutions of the hybrid method.

Appendix A. Proof of Lemma 3.1. Define

$$A_{\mathbf{i},\mathbf{k},\mathbf{i'},\mathbf{k'}} := \left\langle \widehat{\phi}_{\mathbf{i},\mathbf{k}} - \widehat{\phi}^*_{\mathbf{i},\mathbf{k}}, \ \widehat{\phi}_{\mathbf{i'},\mathbf{k'}} - \widehat{\phi}^*_{\mathbf{i'},\mathbf{k'}} \right\rangle.$$

Consider

$$\|f - f^*\|^2_{L^2(\mathbb{R}^d)} = \sum_{\mathbf{i},\mathbf{k},\mathbf{i'},\mathbf{k'}} z_{\mathbf{i},\mathbf{k}} \overline{z_{\mathbf{i'},\mathbf{k'}}} A_{\mathbf{i},\mathbf{k},\mathbf{i'},\mathbf{k'}} \leq \sum_{\mathbf{i},\mathbf{k},\mathbf{i'},\mathbf{k'}} |z_{\mathbf{i},\mathbf{k}} \overline{z_{\mathbf{i'},\mathbf{k'}}} A_{\mathbf{i},\mathbf{k},\mathbf{i'},\mathbf{k'}}|$$

$$\leq \sum_{\mathbf{i},\mathbf{k},\mathbf{i'},\mathbf{k'}} \frac{|z_{\mathbf{i},\mathbf{k}}|^2 + |z_{\mathbf{i'},\mathbf{k'}}|^2}{2} |A_{\mathbf{i},\mathbf{k},\mathbf{i'},\mathbf{k'}}|$$

$$= \sum_{\mathbf{i},\mathbf{k},\mathbf{i'},\mathbf{k'}} |z_{\mathbf{i},\mathbf{k}}|^2 |A_{\mathbf{i},\mathbf{k},\mathbf{i'},\mathbf{k'}}| = \sum_{\mathbf{i},\mathbf{k}} |z_{\mathbf{i},\mathbf{k}}|^2 \sum_{\mathbf{i'},\mathbf{k'}} |A_{\mathbf{i},\mathbf{k},\mathbf{i'},\mathbf{k'}}|$$

$$\lesssim \|f\|^2_{L^2(\mathbb{R}^d)} \sup_{\mathbf{i},\mathbf{k}} \sum_{\mathbf{i'},\mathbf{k'}} |A_{\mathbf{i},\mathbf{k},\mathbf{i'},\mathbf{k'}}|.$$

It suffices to show that, for any fixed $\mathbf{i},\mathbf{k}$, $\sum_{\mathbf{i'},\mathbf{k'}} |A_{\mathbf{i},\mathbf{k},\mathbf{i'},\mathbf{k'}}| \sim \mathcal{O}(1)$.

Fix $\mathbf{i},\mathbf{k}$. Define $\delta\mathbf{k} := \mathbf{k'} - \mathbf{k}$ and $\delta\boldsymbol{\xi} := \boldsymbol{\xi}_{\mathbf{i'}} - \boldsymbol{\xi}_{\mathbf{i}}$. By definition,

$$A_{\mathbf{i},\mathbf{k},\mathbf{i'},\mathbf{k'}} = \frac{1}{L^d} \int_{\mathbb{R}^d} e^{-2\pi i \, \mathbf{k}\cdot\boldsymbol{\xi}/L} \, e^{-|\boldsymbol{\xi}-\boldsymbol{\xi}_{\mathbf{i}}|^2/\sigma^2} \left(1 - \chi\left(\frac{\boldsymbol{\xi}-\boldsymbol{\xi}_{\mathbf{i}}}{2\sigma}\right)\right)$$

$$\cdot \, e^{2\pi i \, \mathbf{k'}\cdot\boldsymbol{\xi}/L} \, e^{-|\boldsymbol{\xi}-\boldsymbol{\xi}_{\mathbf{i'}}|^2/\sigma^2} \left(1 - \chi\left(\frac{\boldsymbol{\xi}-\boldsymbol{\xi}_{\mathbf{i'}}}{2\sigma}\right)\right) d\boldsymbol{\xi}$$

$$= \frac{1}{L^d} \int_{\mathbb{R}^d} e^{-2\pi i \, (\delta\mathbf{k})\cdot\boldsymbol{\xi}/L} \, e^{-|\boldsymbol{\xi}-\boldsymbol{\xi}_{\mathbf{i}}|^2/\sigma^2 - |\boldsymbol{\xi}-\boldsymbol{\xi}_{\mathbf{i'}}|^2/\sigma^2}$$

$$\cdot \left(1 - \chi\left(\frac{\boldsymbol{\xi}-\boldsymbol{\xi}_{\mathbf{i}}}{2\sigma}\right)\right) \left(1 - \chi\left(\frac{\boldsymbol{\xi}-\boldsymbol{\xi}_{\mathbf{i'}}}{2\sigma}\right)\right) d\boldsymbol{\xi}.$$

Using the change of variable $\boldsymbol{\xi} = \sigma z + \boldsymbol{\xi}_{\mathbf{i}}$,

$$A_{\mathbf{i},\mathbf{k},\mathbf{i'},\mathbf{k'}} = \frac{1}{4^d} \int_{\mathbb{R}^d} e^{-2\pi i \, (\delta\mathbf{k})\cdot(\sigma z + \boldsymbol{\xi}_{\mathbf{i}})/L} \, e^{-|z|^2 - |z - \delta\boldsymbol{\xi}/\sigma|^2}$$

$$\cdot \left(1 - \chi\left(\frac{z}{2}\right)\right) \left(1 - \chi\left(\frac{\mathbf{z}}{2} - \frac{\delta\boldsymbol{\xi}}{2\sigma}\right)\right) d\boldsymbol{\xi}.$$

Let $\chi_1(z) = \chi(z/2)$ and $\chi_2(z) = \chi(z/2 - \delta\boldsymbol{\xi}/2\sigma)$. Consider

$$I := \int_{\mathbb{R}^d} e^{-2\pi i \, (\delta\mathbf{k})\cdot(\sigma z + \boldsymbol{\xi}_{\mathbf{i}})/L} \, e^{-|z|^2 - |z - \delta\boldsymbol{\xi}/\sigma|^2} \Big(1 - \chi_1(\mathbf{z})\Big)\Big(1 - \chi_2(\mathbf{z})\Big) d\boldsymbol{\xi}.$$

Defining the differential operator $\mathcal{L} := \frac{1-\Delta}{1+\sigma^2|\delta\mathbf{k}|^2}$, we have

$$\mathcal{L} \, e^{-2\pi i \, (\delta\mathbf{k})\cdot(\sigma z + \boldsymbol{\xi}_{\mathbf{i}})/L} = e^{-2\pi i \, (\delta\mathbf{k})\cdot(\sigma z + \boldsymbol{\xi}_{\mathbf{i}})/L}.$$

Hence, for any positive integer m,

$$I = \int_{\mathbb{R}^d} \left(\mathcal{L}^m e^{-2\pi i \, (\delta\mathbf{k})\cdot(\sigma z + \boldsymbol{\xi}_{\mathbf{i}})/L}\right) \, e^{-|z|^2 - |z - \delta\boldsymbol{\xi}/\sigma|^2} \Big(1 - \chi_1(\mathbf{z})\Big)\Big(1 - \chi_2(\mathbf{z})\Big) d\boldsymbol{\xi}$$

$$= \frac{1}{(1 + \sigma^2 |\delta\mathbf{k}|^2)^m} \int_{\mathbb{R}^d} e^{-2\pi i \, (\delta\mathbf{k})\cdot(\sigma z + \boldsymbol{\xi}_{\mathbf{i}})/L} (1 - \Delta)^m$$

$$\cdot \left(e^{-|z|^2 - |z - \delta\boldsymbol{\xi}/\sigma|^2} \cdot \Big(1 - \chi_1(\mathbf{z})\Big)\Big(1 - \chi_2(\mathbf{z})\Big)\right) d\boldsymbol{\xi}.$$

One can check that

$$\left|(1-\Delta)^m\left(e^{-|z|^2-|z-\delta\boldsymbol{\xi}/\sigma|^2}\Big(1-\chi_1(\mathbf{z})\Big)\Big(1-\chi_2(\mathbf{z})\Big)\right)\right|$$
$$\lesssim e^{-|z|^2-|z-\delta\boldsymbol{\xi}/\sigma|^2}\left(1+\sum_{r=1}^{2m}|z|^r+|z-\delta\boldsymbol{\xi}/\sigma|^r\right)\Big(1-\chi_1(z)\Big).$$

Hence, for any fixed m,

$$|A_{\mathbf{i},\mathbf{k},\mathbf{i}',\mathbf{k}'}|\lesssim|I|\lesssim\frac{1}{1+\sigma^{2m}|\delta\mathbf{k}|^{2m}}\int_{|z|\geq1}e^{-|z|^2-|z-\delta\boldsymbol{\xi}/\sigma|^2}d\boldsymbol{\xi}$$
$$\lesssim\frac{1}{1+\sigma^{2m}|\delta\mathbf{k}|^{2m}}\,e^{-|\delta\boldsymbol{\xi}/\sigma|^2/3}\int_{|z|\geq1}e^{-|z|^2/2}d\boldsymbol{\xi}\lesssim\frac{e^{-|\delta\boldsymbol{\xi}/\sigma|^2/3}}{1+\sigma^{2m}|\delta\mathbf{k}|^{2m}}.$$

Therefore, for any fixed $\mathbf{i},\mathbf{k}$, by taking $m=\left\lceil\frac{d+1}{2}\right\rceil+1$, we have

$$\sum_{\mathbf{i}',\mathbf{k}'}|A_{\mathbf{i},\mathbf{k},\mathbf{i}',\mathbf{k}'}|\lesssim\sum_{\mathbf{i}'\in\mathbb{Z}_{N/W}^d}e^{-|\delta\boldsymbol{\xi}/\sigma|^2/3}\sum_{\mathbf{k}'\in\mathbb{Z}_L^d}\frac{1}{1+\sigma^{2m}|\delta\mathbf{k}|^{2m}}$$
$$\lesssim\int_{\mathbb{R}^d}e^{-|\boldsymbol{\xi}/\sigma|^2/3}\,d\boldsymbol{\xi}\int_{\mathbb{R}^d}\frac{1}{1+\sigma^{2m}|\mathbf{x}|^m}\,d\mathbf{x}\lesssim1.$$

REFERENCES

[1] M. Zworski, *Semiclassical Analysis*, American Mathematical Society, Providence, RI, 2012.

[2] J.-D. Benamou, F. Collino, and O. Runborg, *Numerical microlocal analysis of harmonic wavefields*, J. Comput. Phys., 199 (2004), pp. 717–741.

[3] J. Qian and L. Ying, *Fast Gaussian wavepacket transforms and Gaussian beams for the Schrödinger equation*, J. Comput. Phys., 229 (2010), pp. 7848–7873.

[4] J. Qian and L. Ying, *Fast multiscale Gaussian wavepacket transforms and multiscale Gaussian beams for the wave equation*, Multiscale Model. Simul., 8 (2010), pp. 1803–1837.

[5] J.-D. Benamou, F. Collino, and S. Marmorat, *Numerical microlocal analysis of 2-d noisy harmonic plane and circular waves*, Asymptot. Anal., 83 (2013), pp. 157–187.

[6] J. Fang, J. Qian, L. Zepeda-Nunez, and H.-K Zhao, *Learning dominant wave directions for plane wave methods for high-frequency Helmholtz equations*, Res. Math. Sci., 4 (2017), pp. 9–39.

[7] J. Fang, J. Qian, L. Zepeda-Núnez, and H. Zhao, *A hybrid approach to solve the high-frequency Helmholtz equation with source singularity in smooth heterogeneous media*, J. Comput. Phys., 371 (2018), pp. 261–279.

[8] E. Chung, C. Lam, and J. Qian, *A ray-based IPDG method for high-frequency time-domain acoustic wave propagation in inhomogeneous media*, J. Comput. Phys., 348 (2017), pp. 660–682.

[9] T. Betcke and J. Phillips, *Approximation by Dominant Wave Directions in Plane Wave Methods*, Technical report, University College London, London, 2012.

[10] Y. Landa, N. M. Tanushev, and R. Tsai, *Discovery of point sources in the Helmholtz equation posed in unknown domains with obstacles*, Commun. Math. Sci., 9 (2011), pp. 903–928.

[11] R. Carriere and R. L. Moses, *High resolution radar target modeling using a modified Prony estimator*, IEEE Trans. Antennas and Propagation, 40 (1992), pp. 13–18.

[12] Y. Hua and T. K Sarkar, *Matrix pencil method for estimating parameters of exponentially damped/undamped sinusoids in noise*, IEEE Trans. Acoust. Speech Signal Process., 38 (1990), pp. 814–824.

[13] A. Martinez, *An Introduction to Semiclassical and Microlocal Analysis*, Springer, New York, 2002.

[14] S. Leung and J. Qian, *The backward phase flow and FBI-transform-based Eulerian Gaussian beams for the Schrödinger equation*, J. Comput. Phys., 229 (2010), pp. 8888–8917.

[15] F. Ihlenburg, *Finite Element Analysis of Acoustic Scattering*, Appl. Math. Sci. 132, Springer, New York, 2006.

[16] I. M. Babuška and S. A. Sauter, *Is the pollution effect of the FEM avoidable for the Helmholtz equation considering high wave numbers?*, SIAM J. Numer. Anal., 34 (1997), pp. 2392–2423.

[17] N. C. Nguyen, J. Peraire, F. Reitich, and B. Cockburn, *A phase-based hybridizable discontinuous Galerkin method for the numerical solution of the Helmholtz equation*, J. Comput. Phys., 290 (2015), pp. 318–335.

[18] C. Y. Lam and C.-W. Shu, *A phase-based interior penalty discontinuous Galerkin method for the Helmholtz equation with spatially varying wavenumber*, Comput. Methods Appl. Mech. Engrg., 318 (2017), pp. 456–473.

[19] E. Giladi and J. B. Keller, *A hybrid numerical asymptotic method for scattering problems*, J. Comput. Phys., 174 (2001), pp. 226–247.

[20] R. Hiptmair, A. Moiola, and I. Perugia, *A Survey of Trefftz Methods for the Helmholtz Equation*, preprint, https://arxiv.org/abs/1506.04521 (2015).

[21] R. Hiptmair, A. Moiola, and I. Perugia, *Plane wave discontinuous Galerkin methods for the 2D Helmholtz equation: Analysis of the p-version*, SIAM J. Numer. Anal., 49 (2011), pp. 264–284.

[22] R. Hiptmair, A. Moiola, and I. Perugia, *Plane wave discontinuous Galerkin methods: Exponential convergence of the hp-version*, Found. Comput. Math., 16 (2015), pp. 637–675.

[23] C. J. Gittelson, R. Hiptmair, and I. Perugia, *Plane wave discontinuous Galerkin methods: Analysis of the h-version*, ESAIM Math. Model. Numer. Anal., 43 (2009), pp. 297–331.

[24] L. M. Imbert-Gerard and B. Despres, *A generalized plane-wave numerical method for smooth nonconstant coefficients*, IMA J. Numer. Anal., 34 (2014), pp. 1072–1103.

[25] M. Kline and I. W. Kay, *Electromagnetic Theory and Geometrical Optics*, Interscience, New York, 1965.

[26] H. Jeffreys, *On certain approximate solutions of linear differential equations of the second order*, Proc. Lond. Math. Soc. (3), 2 (1925), pp. 428–436.

[27] L. Rayleigh, *On the propagation of waves through a stratified medium, with special reference to the question of reflection*, Proc. Roy. Soc. Lond. Ser. A, 86 (1912), pp. 207–226.

[28] J. Qian and W. W. Symes, *An adaptive finite difference method for traveltime and amplitude*, Geophysics, 67 (2002), pp. 167–176.

[29] Y. Du and H. Wu, *Preasymptotic error analysis of higher order FEM and CIP-FEM for Helmholtz equation with high wave number*, SIAM J. Numer. Anal., 53 (2015), pp. 782–804.

[30] M. J. Grote, A. Schneebeli, and D. Schötzau, *Discontinuous Galerkin finite element method for the wave equation*, SIAM J. Numer. Anal., 44 (2006), pp. 2408–2431.